Meteorologische Zeitschrift, Vol. **24**, No. 3, 313–342 (published online April 4, 2015)

Article

Towards a Framework for the Stochastic Modelling of Subgrid Scale Fluxes for Large Eddy Simulation

Thomas von Larcher[1*], Andrea Beck[2], Rupert Klein[1], Illia Horenko[3], Philipp Metzner[4], Matthias Waidmann[1], Dimitri Igdalov[3], Gregor Gassner[5] and Claus-Dieter Munz[2]

[1]Institute for Mathematics, Freie Universität Berlin, Germany
[2]Institute of Aerodynamics and Gas Dynamics, University of Stuttgart, Germany
[3]Institute of Computational Science, Università della Svizzera Italiana, Lugano, Switzerland
[4]formerly: Institute of Computational Science, Università della Svizzera Italiana, Lugano, Switzerland
[5]Mathematical Institute, University of Cologne, Germany

(Manuscript received January 27, 2014; in revised form November 25, 2014; accepted November 26, 2014)

Abstract

We focus on a mixed deterministic-stochastic subgrid scale modelling strategy currently under development for application in Finite Volume Large Eddy Simulation (LES) codes. Our concept is based on the integral conservation laws for mass, momentum and energy of a flow field. We model the space-time structure of the flux correction terms to create a discrete formulation. Advanced methods of time series analysis for the data-based construction of stochastic models with inherently non-stationary statistical properties and concepts of information theory based on a modified Akaike information criterion and on the Bayesian information criterion for the model discrimination are used to construct surrogate models for the non-resolved flux fluctuations. Vector-valued auto-regressive models with external influences form the basis for the modelling approach. The reconstruction capabilities of the modelling ansatz are tested against fully 3D turbulent channel flow data computed by direct numerical simulation and, in addition, against a turbulent Taylor-Green vortex flow showing a transition from laminar to a turbulent flow state. The modelling approach for the LES closure is different in both test cases. In the channel flow we consider an implicit LES ansatz. In the Taylor-Green vortex flow, it follows an explicit closure approach. We present here the outcome of our reconstruction tests and show specific results of the non-trivial time series data analysis. Started with a generally stochastic ansatz we found, surprisingly, that the deterministic model part already yields small residuals and is, therefore, good enough to fit the flux correction terms well. In the Taylor-Green vortex flow, we found additionally time-dependent features confirming that our modelling approach is capable of detecting changes in the temporal structure of the flow. The results encourage us to launch a more ambitious attempt at dynamic LES closure along these lines.

Keywords: large eddy simulation, subgrid scale fluxes, modelling strategy, deterministic-stochastic approach

1 Introduction

The integral conservation laws for mass, momentum and energy of a flow field are universally valid for arbitrary control volumes. These laws describe the time evolution of the integral values of the conserved quantities per control volume as a function of the associated fluxes across its bounding surfaces written as

$$\int_Q u_{\partial t}\, dx + \oint_{\partial Q} F(u)\, ds = 0, \tag{1.1}$$

with Q and ∂Q as the control volume and its surface, respectively, u as the conserved quantity, F as its normal flux across ∂Q, and the subscript ∂t denotes the time derivate. The *exact* evolution in time for the mean value of u, denoted by $\bar{u}$, is given by

$$\bar{u}_{\partial t} = -\frac{1}{|Q|} \oint_{\partial Q} F(u)\, ds. \tag{1.2}$$

Thus, if the associated fluxes across its bounding surfaces are determined exactly, the equations capture the underlying physics of conservation correctly and guarantee an accurate prediction of the temporal evolution of the integral mean values. That is, in contrast to Finite Difference, Finite Element or spectral methods, a Finite Volume approach does not introduce any discretization error per se.

In the discrete view, the discretization basis for the Finite Volume approach generally reads

$$\bar{u}_{\partial t} + \frac{1}{|Q|} \oint_{\partial Q} H(\bar{u}^+, \bar{u}^-) ds = 0, \tag{1.3}$$

*Corresponding author: Thomas von Larcher, Institute for Mathematics, Freie Universität Berlin, Arnimallee 6, 14195 Berlin, Germany, e-mail: larcher@math.fu-berlin.de

DOI 10.1127/metz/2015/0581
Gebrüder Borntraeger Science Publishers, Stuttgart, www.borntraeger-cramer.com

with a numerical flux function $H(\bar{u}^+, \bar{u}^-)$, where the arguments $\bar{u}^+$ and $\bar{u}^-$ result from a suitable spatial reconstruction of the mean values, u again as the conserved quantity and superscripts $^+$ and $^-$ as the specific cell face side. Thus, a discretization error is introduced into the evolution of $\bar{u}$ if $H(\bar{u}^+, \bar{u}^-) \neq F(u)$.

In terms of a coarse scale simulation method, a natural scale separation can be written as

$$u := \bar{u} + u', \tag{1.4}$$

with $\bar{u}$ (u') as quantity at the coarse scale (subgrid/small scale). In the same spirit, an induced flux separation can be written as

$$F(u) := H(\bar{u}^+, \bar{u}^-) + \Delta F, \tag{1.5}$$

with $H(\bar{u}^+, \bar{u}^-)$ as the coarse flux, superscripts $^+$ and $^-$ denote the specific cell face side, and ΔF as the flux correction term. Thus, it requires the reconstruction of the flux correction terms, i.e. of the subgrid fluxes, to get the exact evolution of the mean values.

Since the pioneering results by A.N. Kolmogorov, Kolmogorov (1941), Kolmogorov (1962), that small eddies in high Reynolds number turbulent flows are universal, cf. also Oboukhov (1962), Lesieur (1987), scientists are encouraged to model the SGS stress tensor, which links the resolved eddies on the large scales (larger than a specific filter width) and the unresolved eddies on the small scales (smaller than that filter width), see, e.g. Sagaut (2006), and a number of models, usually classified as eddy viscosity models and synthetic field models were developed in the past. The former, e.g., the prominent Smagorinsky model approach, Smagorinsky (1963), are constrained by the fact that they are typically only poorly correlated with the real physics of the subgrid scale flow. Moreover, they are not able to represent the energy backscatter process which can be of relevance in applications, especially in meteorological flows. We refer to the paper e.g. by Rogallo and Moin (1984) for a thorough review of the requirements for the numerical simulations of turbulent flows. Stochastic forcing approaches were developed to handle the backscatter problem, e.g., Leith (1990), Schumann (1995). Synthetic field models consider the real physics of the small scale eddies and, therefore, might be more promising. There are a number of different synthetic field modelling approaches, for example similarity models, e.g., Liu et al. (1994), stretched vortex models, e.g., Misra and Pullin (1997), phase estimation models, e.g., Domaradzki and Saiki (1997), and fractal models, e.g., Scotti and Meneveau (1999). A dynamic procedure in LES based on a Finite Volume integral has been recently introduced in Denaro and De Stefano (2011), and a novel approach in LES modelling of turbulent channel flow is the so-called LES with stochastic subgrid acceleration models (LES-SSAM), Zamansky et al. (2013), recently introduced by Sabel'nikov et al. (2011). Despite the progress that has been made, determining a suitable subgrid scale model remains a challenging and intriguing task.

In this paper, we introduce a new promising methodology for data-based model extraction to LES-modelling in preparation of a novel LES closure approach. The method is based on a mixed deterministic-stochastic modelling ansatz based on the integral conservation laws. We demonstrate that this technique yields meaningful results for well-established turbulence modelling reference flows, that is, firstly, a turbulent channel flow and, secondly, a Taylor-Green vortex (TGV) flow.

With respect to (1.5), we directly aim at flux correction terms, ΔF, to correct for the influence of the non-resolved small scale information and model the temporal structure of the fluxes to create a discrete formulation. The approach is similar in spirit to earlier propositions, e.g., Scotti and Meneveau (1999), but differs in terms of both the stochastic modelling ansatz and of the underlying combined Discontinuous Galerkin-Finite Volume approximation framework, e.g., Gassner and Beck (2013).

Moreover, our approach particularly allows for the analysis of non-stationary and non-homogeneous data. In contrast, stationary and homogeneous statistics, e.g. first order (mean) and second order (variance) statistics, often used in data analysis representations, do imply constraints and could lead to biased results, as those moments typically do not represent the characteristics of inhomogeneous/non-stationary data.

We realize non-stationary statistical properties of these models by allowing for time dependent switches between different fluctuation regimes, also called and hereafter referred to as local models, which are represented by different, but fixed, sets of model parameters. **V**ector-valued **A**uto-**R**egressive models with e**X**ternal influences (VARX-models) form the basis for this approach. In constructing the VARX surrogate model using information criteria, our method corroborates the central assumption of most LES schemes that local closures can safely rely on next-neighbor stencil information only, that is the LES grid averaged conserved quantities in the immediate vicinity of a given LES grid cell interface are incorporated as external influences. In this fashion our model ansatz incorporates the information available from a typical numerical discretization stencil as would be used, e.g., in formulating a classical Smagorinsky closure.

The outline of the paper is as follows. In the next section we describe the deterministic-stochastic data-based modelling approach and the time series analysis framework. The data generation and pre-processing procedure for both test cases is part of Section 3. Results of the reconstruction tests are shown in Section 4 and are discussed in Section 5. The paper then ends with some concluding remarks and an outlook onto future work (Section 6).

2 Modelling approach

Our approach, (cf. Horenko (2010a)), makes use of advanced methods of time series analysis based on the family of VARX-models and used for the data-based construction of stochastic models with inherently non-stationary statistical properties. More precisely, the approach makes use of Finite-Element Method (FEM)-based time series analysis with bounded variation (BV) of model parameters, and it allows for the simultaneous dimension reduction and identification of dynamical models with external factors.

The VARX model in its general form is a simple yet sufficiently complex model widely used to investigate dynamical multivariate time series, cf. Krolzig (2000). It arises from the assumption that the dynamics of a time series $P = (p_t)$, $p_t \in \mathbb{R}^n$, $t = 0, \ldots, T$ under consideration is governed by a VARX function which additionally depends on external factors $U = (u_t)$, $u_t \in \mathbb{R}^k$, $t = 0, \ldots, T$. Please note, that the subscript t denotes the time and not the time derivative.

Formally, the non-stationary non-linear VARX-model reads

$$p_t = \mu(t) + \mathbf{A}(t)\phi_1(p_{t-1}, \ldots, p_{t-m}) + \mathbf{B}(t)\phi_2(u_t) + \varepsilon_t, \quad (2.1)$$

($t = m, \ldots, T$), and the most simple and straightforward form of the VARX-model is the *linear autoregressive factor model* with ϕ_1 then as the identity operator ($\phi_1(\cdot) = \mathrm{Id}(\cdot)$) (cf. Brockwell and Davis (2002))

$$p_t = \mu(t) + \sum_{q=1}^{m} \mathbf{A}_q(t) p_{t-q} + \mathbf{B}(t)\phi_2(u_t) + \varepsilon_t. \quad (2.2)$$

In (2.1) and (2.2), ε_t is a multivariate random variable with zero expectation, $\mathbb{E}[\varepsilon_t] = 0$, allowing for the modelling of noise, $(\mu, \mathbf{A}, \mathbf{B})(t)$ are time-dependent parameters consistently sized with respect to the dimension of the time series (p_t), and $\phi_1(\cdot)$ and $\phi_2(\cdot)$ are (non-)linear model ansatz functions. m denotes the memory-depth allowing for consideration of the time series' history.

Note, that the models are called stochastic because the general model ansatz includes the above mentioned stochastic noise term, ε_t, to model the statistics of the residuals left when only considering the deterministic part of the scheme. ε_t can be also interpreted as model-data-discrepancy.

2.1 Specific FEM-BV-VX approach

As already mentioned, our specific modelling ansatz focuses on unresolved subgrid scale flux correction terms, and we will use it to construct surrogate models for the non-resolved flux fluctuations from specific time series. Following (2.1), the VARX model, variable in time, t, and space, $\vec{x}$, now reads

$$\Delta F_{\text{exact}} = \mu(t, \vec{x}) + \mathbf{A}(t, \vec{x})\phi_1(\Delta F_{t-\tau}, \ldots, \Delta F_{t-m\tau})_{\vec{x}} + \mathbf{B}(t, \vec{x})\phi_2(u_{t,\vec{x}}) + \varepsilon_{t,\vec{x}}, \quad (2.3)$$

with ΔF_{exact} as the exact flux corrections to be modelled and ΔF as numerical flux corrections. $(\mu, \mathbf{A}, \mathbf{B})(t, \vec{x})$ and ϕ_1, ϕ_2 are, again, the model parameters and the model ansatz functions, and $u_{t,\vec{x}}$ and $\epsilon_{t,\vec{x}}$ represents the external influences and the random variable.

It is one key result of our work that, in the context of our approach, it turned out after application of information criteria described in the following that the general model in (2.3) simplifies considerably. An extensive study based on the mAIC-metric (described below) shows that the optimal model for the two test cases is the VX-approach instead of the VARX-ansatz. That is, our modelling approach under consideration does not include auto-regressive terms as anticipated above.

Moreover, we surprisingly found that the residuals left when only the deterministic part is considered are very small so that there is no need to evaluate the term ε_t in our ansatz. Regarding the modelling approach for the flux correction per cell j, j as cell index, the employed (customized) VX-model, i.e. without auto-regression, then reads

$$\Delta F_{\text{fitted}}\left(u_t^j, \mu^j(t), \mathbf{B}^j(t)\right) := \mu^j(t) + \mathbf{B}^j(t)\phi(u_t^j) \quad (2.4)$$

where ΔF_{fitted} now represents the RHS of (2.3). Here, the function $\phi(\cdot)(\equiv \phi_2(\cdot))$ allows for linear or nonlinear influences of the surrounding cell average on the flux corrections. Note, that also the stochastic term ε_t is dropped, now, as we are not interpreting it statistically.

Generally, choosing $\phi(u) = u$, $u \in \mathbb{R}^k$, results in an affine linear VX-model taking only first order correlations of the data into account. To incorporate second order correlations, we consider

$$\phi(u) = (u_1, \cdots, u_k, u_1u_1, u_1u_2, \ldots, u_1u_k, u_2u_3, \ldots, u_ku_k) \in \mathbb{R}^{k+\frac{k(k+1)}{2}}. \quad (2.5)$$

The aim of our modelling ansatz is to find the optimal parameters that describe the best-fit model which then represents the time series of the exact flux correction term. With the model parameters and the external influences given, our approach allows for the construction of local models, each being represented by a particular set of (fixed) model parameters and, also, for time dependent switches between those local models to (best-)fit the exact flux correction time series.

In that fashion, the model parameters, $(\mu, \mathbf{B})(t, \vec{x})$, are represented by $\mathbf{K}$ local models of k (local) parameters $\{\Theta_i \equiv (\Theta_1, \ldots, \Theta_k)_i\}_{i=1}^{\mathbf{K}}$, and the time dependent switches between the local models are represented by model affiliation functions $\gamma_j(t, \vec{x})$, also called time-dependent weights.

In the line of the FEM-BV-approach, the *average cluster functional* (an effective error measure) associated

with (2.4) reads

$$\mathbf{L}(\mathbf{K},\mathbf{C}) = \sum_{j=1}^{N}\sum_{i=1}^{\mathbf{K}}\sum_{t=0}^{T}\gamma_i^j(t)\left\|\Delta F^j_{\text{exact}}(t) - \left[\Delta F_{\text{fitted}}(u_t^j,\mu_i^j,\mathbf{B}_i^j)\right]\right\|_2^2 \tag{2.6}$$

with $\gamma_i^j(t)$ subject to the constraints ($j = 1,\ldots,N$, $i = 1,\ldots,\mathbf{K}$, $t = 0,\ldots,T$)

$$\left\|\gamma_i^j\right\|_{BV} = \sum_{t=0}^{T-1}|\gamma_i^j(t+1) - \gamma_i^j(t)| \le \mathbf{C}, \tag{2.7}$$

$$\sum_{i=1}^{\mathbf{K}}\gamma_i^j(t) = 1, \tag{2.8}$$

$$\gamma_i^j(t) \ge 0, \tag{2.9}$$

$\mathbf{C}$ as persistence threshold and (2.7) denotes the persistency condition in the time-discrete BV-sense. Note, that the term $\mathbf{L}(\mathbf{K},\mathbf{C})$ in (2.6) denotes the likelihood and represents the model distance function expressed by a linear combination of local model distance functions.

With this, the aim of the modelling approach now is to find the optimal parameters and the optimal affiliation functions, (Θ^*,γ^*), i.e. the optimal number of local models $\mathbf{K}$ and the optimal persistence threshold $\mathbf{C}$. With a given set of parameters $(k,\mathbf{K},\mathbf{C})$, we have, therefore, to minimize

$$\mathbf{L}(\mathbf{K},\mathbf{C})_{t,\vec{x}} \to \min_{\gamma,\Theta} \tag{2.10}$$

in determining the optimal parameters.

The model affiliation functions $\gamma_i(t,\vec{x})$ are defined as in (2.7) and are represented by the FEM-BV-method, i.e. they are approximated in time by a linear combination of functions, following the ansatz

$$\gamma_i(t) = \sum_{n=1}^{N}\alpha_{in}\phi_n(t), \tag{2.11}$$

with $\phi_n(t)$ as Finite Element (piecewise constant) ansatz functions, and regularized by (2.7–2.9). With this, we are able to estimate the parameters of the local models and the switching processes by the FE method.

The balance between the requirements of high representation quality and low number of free parameters $(\mathbf{K},\mathbf{C})$ (Occam's razor) is achieved by involving criteria from information theory. In case of the channel flow, our approach makes use of the so-called modified Akaike Information Criterion (mAIC), Metzner et al. (2012), to find the optimal model. The AIC has been originally developed by Akaike (1974). Besides from other advantages, the mAIC specifically allows for the *simultaneous* identification of the optimal parameters, and the optimal model is then related to that model which minimizes the mAIC.

The mAIC reads

$$mAIC(\mathbf{K},\mathbf{C}) = -2\ln(\mathbf{L}(\mathbf{K},\mathbf{C})) + 2|M(\mathbf{K},\mathbf{C})|, \tag{2.12}$$

with $|M(\mathbf{K},\mathbf{C})|$ as the total number of the model's free parameter. For example, if $\mathbf{K} = 1$ (stationarity), $|M(\mathbf{K},\mathbf{C})| = |\Theta|$. If $\mathbf{K} > 1$ (non-stationarity), $|M(\mathbf{K},\mathbf{C})|$ = # local models × (# local parameters + # basis functions of the FE) $(\mathbf{K}\times(|\Theta| + \mathbf{C}))$.

In addition to the mAIC, we also make use of a second established information criterion that is the Bayesian information criterion (BIC) to select a proper model for the modelling ansatz. The BIC is generally robust (McQuarrie and Tsai (1998)) and has been successfully applied in a number of studies, e.g. Majda et al. (2006), Franzke et al. (2007). For a local model i, its general form reads (cf. Horenko (2010b))

$$BIC(i) = -2\log(\mathbf{L}_i) + N_i\log\left(\sum_{t=0}^{T}\gamma_i(t)\right), \tag{2.13}$$

with N_i as the number of model parameters in the local model state i. Similar to the mAIC, the model with the lowest value of BIC is the optimal model. Note, that both information criteria are applied in evaluating the optimal parameters in our test cases. We refer the reader also to e.g. Burnahm and Anderson (2002) for a detailed description of AIC and BIC.

The algorithmic framework described here is extensively discussed in Horenko (2010b) and Metzner et al. (2012). It is worth mentioning that this stochastic model approach has been successfully applied in the field of Meteorology and Climatology, too, e.g. Franzke et al. (2009), Horenko (2010b), Blume et al. (2012), O'Kane et al. (2012), O'Kane et al. (2013a), and O'Kane et al. (2013b).

3 Test cases: Data generation and model parameters

The reconstruction capabilities of our modelling approach are tested against two turbulent flows, namely, first, the 3D turbulent channel flow data computed by DNS for an incompressible, isothermal fluid at Reynolds number $Re_\tau = 590$. Secondly, we test against the 3D non-stationary Taylor-Green vortex (TGV) flow data at $Re = 1600$. At this Reynolds number, the TGV flow results in a transition from laminar to fully turbulent flow and, therefore, is a well suited test case for a non-stationary flow phenomena. In the TGV flow test case, the flux correction terms are created during the DNS simulation as the difference between the fully resolved fluxes and their representation by an associated Finite Volume approximation. The flux correction terms are then approximated by different types of viscosity. Therefore, this approach can be considered as an explicit LES closure approach. In the turbulent channel flow test case, the approach makes use of a combination of numerical

flux functions of different order which are used for modelling the exact flux correction term. It, therefore, is an implicit ansatz which deals with the specific discretization.

In context with Section 2.1, in the turbulent channel flow test case, we find that it is sufficient to fit the cells' time series of exact LES corrections $\Delta F^j_{\text{exact}}(t)$ by means of an affine linear function that depends only on the cells' available LES observables $u^j(t)$. With respect to (2.4), the term $\mathbf{B}\phi(u)$ then comprises the above mentioned flux correction terms derived from classical Finite Volume numerical flux functions of different order, specifically 1st-, 2nd-, and 3rd-order (WENO-scheme),

$$\mathbf{B}\phi(u) = \left(b_1\Delta F^{1\text{st}} + b_2\Delta F^{2\text{nd}} + b_3\Delta F^{\text{WENO}} + b_{\text{lin}}\Delta F^{\text{lin}}\right)(u), \tag{3.1}$$

(here the cell index, j, is dropped) with a next-neighbour stencil for $\Delta F^{\text{lin}}(u)$, and the term (u) incorporates coarse-grid stencil data as described in the next section. Thus, the resulting best-fit model takes the form of a stencil-based LES-closure that determines the flux corrections in the turbulent flow regime just from the cell-averages in a finite number of grid cells surrounding the considered grid cell interface.

For the Taylor-Green vortex test case, the term $\mathbf{B}\phi(u)$ incorporates the different dissipation fluxes, d^k, computed from the classical Smagorinsky eddy viscosity and the dissipation matrices of commonly used Finite Volume flux functions. Following the ansatz for the turbulent channel flow, (3.1), the mean velocities of the next-neighbour stencil data are also included as an external factor V, leading to

$$\mathbf{B}\phi(u) = \left(b_1 d^1 + b_2 d^2 + b_3 d^3 + b_4 V\right)(u) \tag{3.2}$$

as the modelling ansatz for the Taylor-Green vortex flow test.

3.1 Turbulent channel flow: Data generation

The turbulent channel flow data we use here for our test bed were previously computed by M. Uhlmann, cf. Uhlmann (2000b). A detailed description of data production is out of the scope of this paper but is given in Uhlmann (2000a). Hence, we give a summary here only and refer the reader to the references.

The data are generated by 3D direct numerical simulation (DNS) of an incompressible, isothermal plane channel flow. A pseudo-spectral Fourier-Chebyshev method similar to Jimenez and Moin (1991), Kim et al. (1987) and Moser et al. (1999) with Chebyshev-tau formulation in wall-normal direction and Fourier representation in the other directions is used. A third order Runge-Kutta based approach is used for time discretization of the non-linear convective terms and an implicit Euler approach is used for the viscous terms. The boundary condition at the side walls in y-direction, normal to the main flow in x-direction, are rigid wall no-slip conditions, and periodic boundaries are defined along the other two (x, z)-axes. Fig. 1 illustrates the channel geometry and its boundary conditions. Details of the numerical approach are given in Klein and Uhlmann (2000) and Uhlmann (2000c).

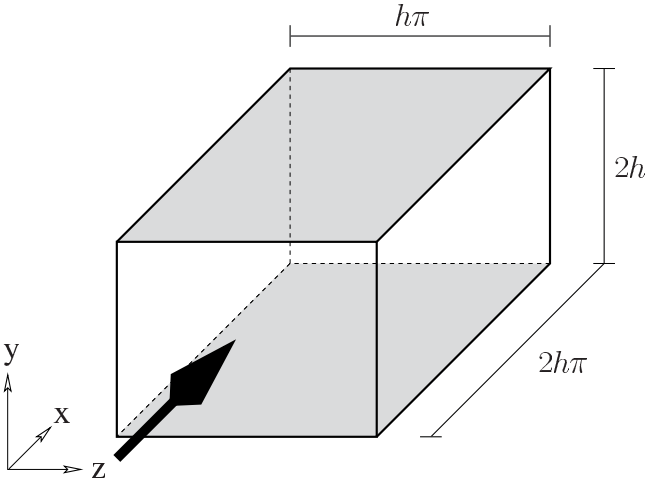

Figure 1: Sketch of the channel flow geometry. The in- and outflow is in x-direction, and rigid wall boundaries are defined in y-direction, and periodic boundaries are defined in x- and z-direction. The scaling parameter h is set to $h = 1$.

The corresponding parameters chosen in the simulation run for computing the turbulent channel flow are given in Table 1. For the purpose of generality, specific Reynolds numbers Re, i.e. friction-velocity based (Re_τ), centreline-velocity based (Re_0), and bulk-velocity based (Re_b), are defined as follows:

$$Re_\tau = \frac{u_\tau \cdot h}{\nu}, \quad Re_b = \frac{U_b \cdot h}{\nu}, \quad Re_0 = \frac{U_0 \cdot h}{\nu}, \tag{3.3}$$

with U_0 as the centreline velocity and U_b as the bulk velocity that reads

$$U_b = \frac{1}{2h} \cdot \int_0^{2h} U(y)dy. \tag{3.4}$$

Here, u_τ is the shear velocity, $u_\tau = \sqrt{\tau_w}$, with τ_w as the wall shear stress, ν is the kinematic viscosity of the fluid, h is the channel half width, and U is the velocity.

The non-stationary Navier-Stokes equations are solved for the wall normal vorticity $\eta = \partial_z u - \partial_x w$, with (u, v, w) as the velocity components in (x, y, z), and the Laplacian of the wall-normal velocity $\varphi = \nabla^2(v)$. The data set which we apply in this study consists of snapshots at 240 particular time steps in terms of the wall-unit time $\Delta t^+ = 1$, where $t^+ = \frac{t \cdot u_\tau^2}{\nu}$. The spatial resolution is $600 \times 385 \times 600$ in (x, y, z).

In a first pre-processing step, the original 3D velocity field is re-computed from the DNS data. This procedure results in three velocity components in each grid point with Chebyshev-distributed grid points in wall-normal

Table 1: Parameters of the channel flow DNS data. Re_τ, Re_0, and Re_b denote the friction-velocity-based, centreline-velocity-based and bulk-velocity-based Reynolds number, L_x and L_z the length and width of the channel. $N_{x,y,z}$ are the number of modes, and $\Delta^+_{x,y,z}$ are the equivalent grid sizes (note, that Δ^+_y is the maximum grid size close to the channel centre).

Re_τ	Re_0	Re_b	L_x	L_z	N_x	N_y	N_z	Δ^+_x	Δ^+_z	Δ^+_y
590	12486	10972	2πh	πh	600	385	600	6.1	3.0	4.8

direction (along the y-axis) and equidistant grid points in the other spatial directions (x-, z-axis). With those data at hand, we are able to compute, for a given LES-grid, a so-called exact flux (F_{ex}), a reference flux (F_{ref}) and numerical fluxes of particular order (F_1, F_2, F_3).

In the line of our study, the approximated fluxes F_1, F_2, F_3 and F_{ref} are not computed on the original grid but are determined based on average velocity data on a Cartesian Finite Volume grid with equidistant spacing in all coordinates, hereafter referred to as the *coarse grid*. Fig. 2 shows exemplarily snapshots of the original velocity data, and of the velocity data re-sampled on the coarse grid. Note, that the exact flux is computed on the original grid. The coarse grid's resolution is similar to that of a LES, whereas LES of wall bounded flows typically would use grid stretching in wall normal direction to satisfy $\Delta y^+ \approx 1$ with y^+ as the wall unit in wall normal direction. In a second pre-processing procedure, both the Finite Volume interface fluxes and the time integration are computed based on the recovered velocity field. Then, flux corrections $\Delta F_1 = (F_1 - F_{\text{ref}})$, $\Delta F_2 = (F_2 - F_{\text{ref}})$, $\Delta F_3 = (F_3 - F_{\text{ref}})$ and $\Delta F_{\text{ex}} = (F_{\text{ex}} - F_{\text{ref}})$ can be calculated. Though the pre-processing framework is a crucial part in our work we skip its detailed description here to retain the legibility of the manuscript and refer the reader to Appendix A where specific details of that procedure are given.

Having applied the pre-processing procedure, the computed flux correction data for the channel flow test case are now available and ready for analysis within the stochastic model framework, and we will present the results in Section 4.1.

3.2 Taylor-Green vortex flow

3.2.1 Flow description

As the second test case for our stochastic approach, we choose the well-known three-dimensional Taylor-Green vortex flow. Originally proposed by Taylor and Green (1937) as a mechanism of producing a scale cascade, this flow evolves from laminar initial conditions through transition into a turbulent field with a wide range of temporal and spatial vortical scales. Beyond a Reynolds number of $Re_{\text{Crit}} \approx 1000$, a turbulent kinetic energy spectrum with the expected $k^{-\frac{5}{3}}$-slope in the inertial subrange develops (cf. Brachet et al. (1983)). Due to the periodic boundary conditions on all outer sides of the cubical domain, the flow field retains its initial symmetries and becomes homogeneous and isotropic in the x-y-plane. Since no kinetic energy production at the large scales exists due to the absence of a mean shear or forcing term, the vortical structures finally decay and the energy cascade subsides.

The initial flow conditions in a triple periodic box of length 2π are given by

$$\begin{aligned} \rho &= \rho_0 = 1, \\ v_1 &= V_0 \sin(x_1)\cos(x_2)\cos(x_3), \\ v_2 &= -V_0 \cos(x_1)\sin(x_2)\cos(x_3), \\ v_3 &= 0, \\ p &= p_0 + \frac{\rho_0 V_0^2}{16}\left(\cos(2x_1) + \cos(2x_2)\right)\left(\cos(2x_3) + 2\right), \end{aligned} \tag{3.5}$$

where ρ, v_i with $i = 1 \ldots 3$ and p denote the density, the components of the velocity vector and the pressure, respectively. While this initial field satisfies the incompressible Navier-Stokes equations, we simulate the flow with a compressible flow solver. We set the Mach number Ma to 0.1, thereby mimicking an essentially incompressible behaviour. Comparisons with published data of incompressible simulations (see Gassner and Beck (2013)) justify this approach. Fig. 3 shows the development of this flow at $Re = 5000$ from an initial mono-scale state to a full multi-scale problem with final dissipative decay. As noted by Brachet et al. (1983), the initial development of the flow is governed by inviscid roll-up and stretching of the vortical structures. At about $t = 3$ in non-dimensional time units, an onset of instability is observed, which leads to the successive breakdown of the coherent structures. This breakdown is complete at about $t = 9$, from whereon the flow is fully turbulent and decays due to lack of large-scale production. During the whole development, the flow retains its spatial isotropy in the x-y-plane and exhibits a strong non-stationary temporal behaviour, thereby complementing the channel flow test case described in Section 3.1 which shows anisotropy in space, but stationarity in time. Thus, our test cases offer different challenges for the FEM-BV-VX approach and allow an assessment of both its spatial model identification features as well as its ability to account for non-stationarity.

Fig. 4 *left* depicts the spectrum of the turbulent kinetic energy after the transitional phase and shows the multi-scale character of this flow with the development of a distinct inertial subrange. The plot in Fig. 4 *right*

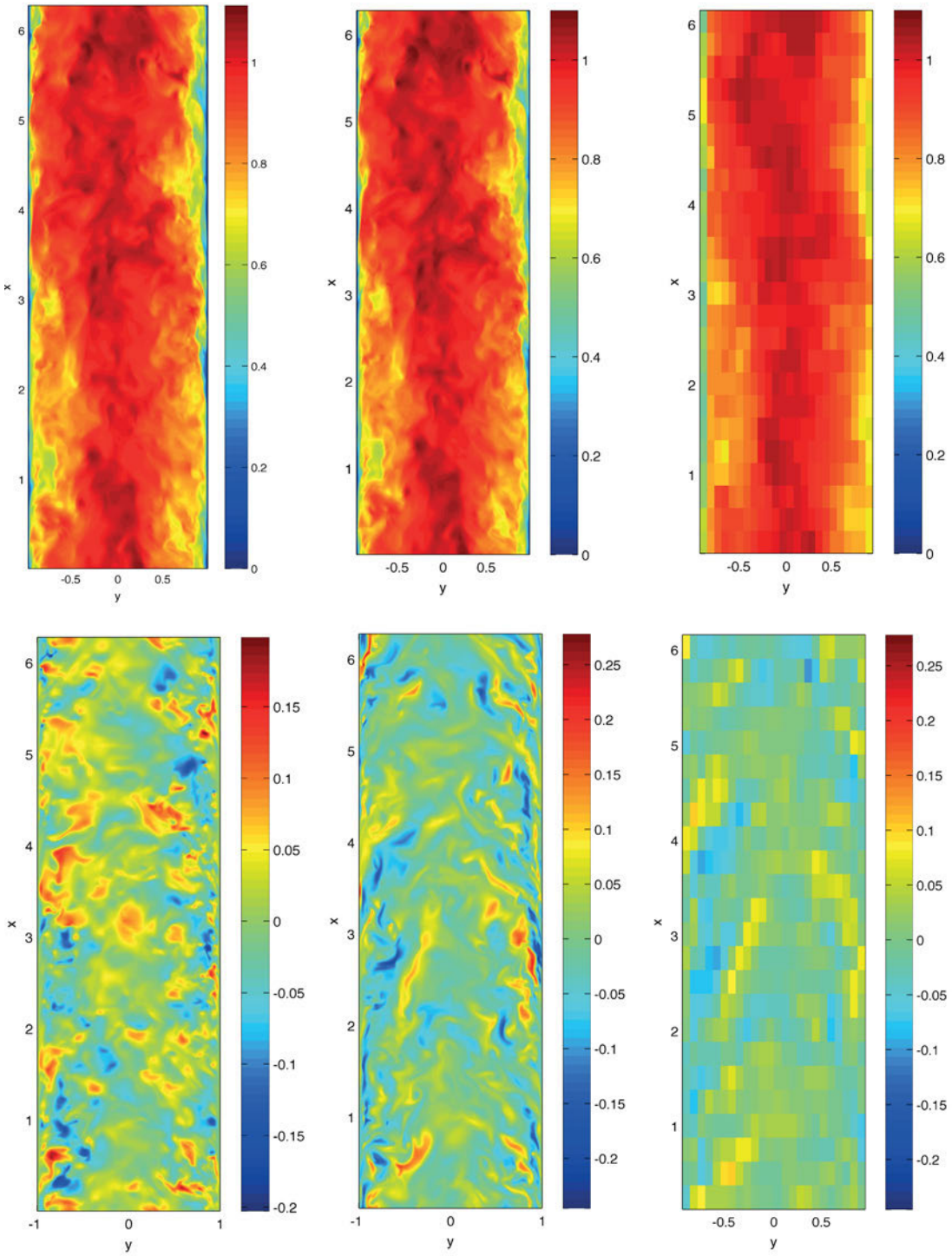

Figure 2: *x*-*y*-slices of the velocity field at $z = \frac{\pi}{2}$ (channel center) at $t = 183.0932\ s$. *Upper row*: *x*-velocity component of the original DNS data (*left*) and of coarse grid re-sampled data (*right*), middle panel: fine grid re-sampled data (cf. Appendix A). *Lower row*: DNS data for the *y*- and *z*-component (*left* and *centre*), and re-sampled coarse grid data of the *z*-velocity component (*right*). The data are given in non-dimensional units. The dimension on the fine (coarse) grid is $600 \times 350 \times 600$ ($25 \times 25 \times 25$) in (x, y, z), the dimension of the original grid is $600 \times 385 \times 600$. Note the equal scaling of the velocity values at the panels in the upper row.

emphasizes the non-stationary behaviour of this flow by showing the evolution of the kinetic energy dissipation through the development of the scale cascade from the laminar initial state through the transition to turbulence and the final viscous decay.

Due to its easily reproducible initial and boundary conditions yet complex physical behaviour, the Taylor-Green vortex flow is a widely used benchmark for both DNS and LES simulations (see, e.g., Drikakis et al. (2007) and Brachet (1991)).

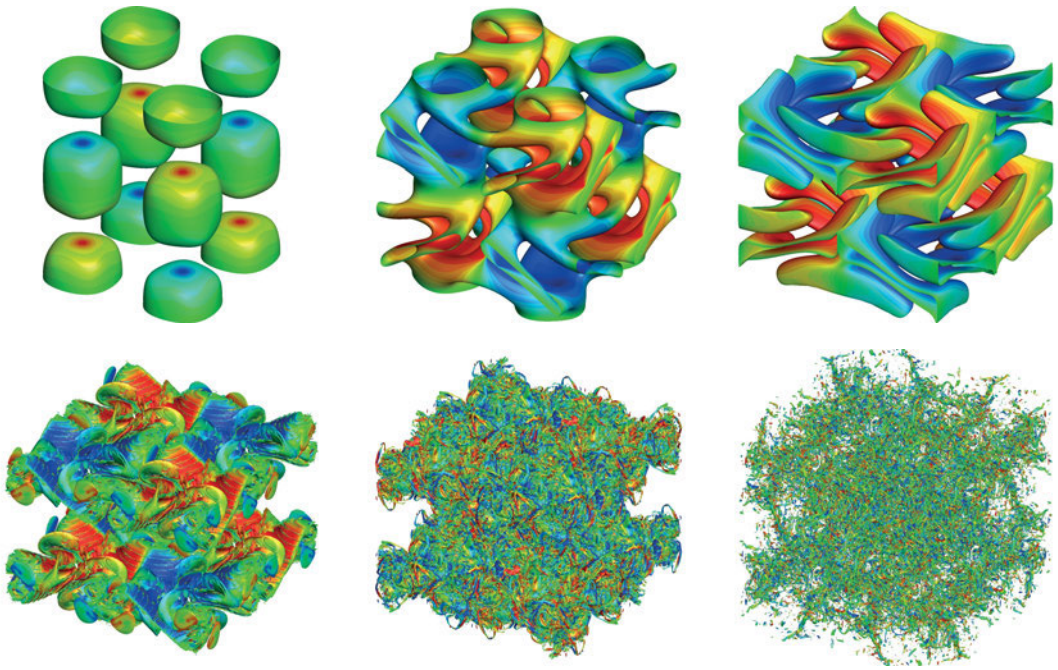

Figure 3: Temporal evolution of the Taylor-Green vortex, from upper left to lower right at non-dimensional time $t = 0.4, 1.4, 2.7, 5.9, 8.9$ and 15.5 (Contours of vorticity, coloured by relative helicity).

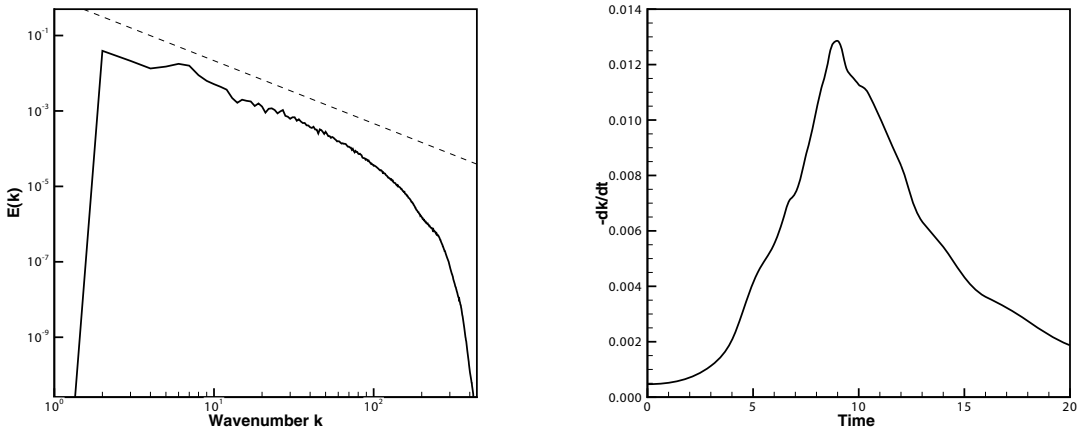

Figure 4: Taylor-Green vortex flow. *Left:* Spectrum of kinetic energy for $Re = 5000$ at $t = 9.0$, dashed line: $k^{-5/3}$slope; *Right:* Rate of kinetic energy dissipation for $Re = 1600$ over non-dimensional time.

3.2.2 Modelling approach

Our modelling approach for the LES closure is complementary to the approach described for the channel flow in Section 3.1. Instead of modelling the LES flux correction term $\Delta F^j_{\text{exact}}(t)$ based on the flux correction terms of different order (see (3.1)), we choose different types of viscosity to approximate the flux correction (see (3.2)). In that sense, this approach is more akin to an explicit LES closure which introduces explicit dissipation terms to account for the unresolved scales, while the previous approach for the modelling of the channel data veers towards an implicit LES method, in which the discretization itself in the form of numerical flux functions of different order is used as a subgrid closure.

As for the channel flow, we choose a FEM-BV-VX approach to model the flux correction from available data as

$$\begin{aligned}\Delta F(u^j(t)) &= F_{\text{ex}}(u^j(t)) - F_{\text{central}}(\bar{u}^j(t)) \\ &= \sum_{i=1}^{\mathbf{K}} \gamma_i^j(t)\left(\mu_i(t) + \mathbf{B}_i(t)(\bar{u}^j(t))\right). \qquad (3.6)\end{aligned}$$

We compute the left hand side of (3.6) as the difference between the exact flux and its approximation by a central Finite Volume flux based on a linear reconstruction (3.11). Since a central flux formulation does not introduce numerical dissipation, it is a natural reference flux for the evaluation of a closure strategy based on explicitly added dissipation terms. As model input

functions on the right hand side, we choose the dissipation introduced by the numerical flux functions and a Smagorinsky eddy viscosity model (cf. Smagorinsky (1963)), along with the averaged velocities of the direct neighbour cells:

$$\begin{aligned}\mathbf{B}_i(t)(\bar{u}^j(t)) &= \sum_{k=1}^{2} \mathbf{C}_i^k(t)\left[g^k(\bar{u}^{j+},\bar{u}^{j-}) - F_{\text{cent}}(\bar{u}^j)\right] + \\ &\quad \mathbf{C}_i^3(t)\,(F_{\text{SGS}}\,(\bar{u}^j,\nabla\bar{u}^j) + \mathbf{A}^i(t)(\bar{u}^{j,n}(t)), \\ &= \sum_{k=1}^{2} \mathbf{C}_i^k(t) D^k[\bar{u}] + \\ &\quad \mathbf{C}_i^3(t)\,(F_{\text{SGS}}\,(\bar{u}^j,\nabla\bar{u}^j) + \mathbf{A}^i(t)(\bar{u}^{j,n}(t)),\end{aligned} \tag{3.7}$$

where $\mathbf{C}$ and $\mathbf{A}$ are the unknown model parameters, D^k is the dissipation matrix of the flux function k defined below, j denotes the analysis cell in our discretization and g represents a numerical flux function. The term F_{SGS} denotes a subgrid scale model flux, in our case, we have chosen the contribution of the classical Smagorinsky model to the viscous fluxes:

$$F^l_{\text{SGS}}(\bar{u},\nabla\bar{u}) = \begin{pmatrix} 0 \\ \tau_{1l} \\ \tau_{2l} \\ \tau_{3l} \\ \tau_{lj}v_j - q_l \end{pmatrix}, \quad l = 1,2,3. \tag{3.8}$$

with the stress tensor based on the velocity field $\vec{v}$ as

$$\underline{\tau} := \mu_{\text{SGS}}(\nabla\vec{v} + (\nabla\vec{v})^T - \frac{2}{3}(\nabla\cdot\vec{v})\underline{I}) \tag{3.9}$$

and the viscosity coefficient μ_{SGS} computed as proposed by Smagorinsky as

$$\mu_{\text{SGS}} = \rho\,(C_s\Delta)^2|\mathbf{S}|. \tag{3.10}$$

$\mathbf{S}$ denotes the strain rate tensor, Δ a suitable filter width and C_s a real constant. In (3.7), the term $\bar{u}^{j,n}(t)$ denotes the cell-averaged values of the velocity components v_1, v_2, v_3 of the analysis cell j and of its directly adjacent neighbours. In our approach, we formulate the Finite Volume scheme for hexahedral elements of a Cartesian grid, so each cell has two neighbouring cells per physical dimension x, y, z, indicated by $n \in [x^+, x^-, y^+, y^-, z^+, z^-]$. The central flux is computed as:

$$F_{\text{cent}}(\bar{u}^j) = \frac{1}{2}\left(F(\bar{u}^{j+}) + F(\bar{u}^{j-})\right) \tag{3.11}$$

with F being the vector of the normal component of the inviscid fluxes. For the numerical flux function $g^k(\bar{u}^{j+},\bar{u}^{j-})$, we choose the local Lax-Friedrichs flux ($k = 1$) (cf. Toro (1999)) and Roe's approximate Riemann solver ($k = 2$) (cf. Roe (1981)).

Local Lax-Friedrichs flux function

The Local Lax-Friedrichs or Rusanov flux function is given by

$$\begin{aligned}&g^1(\bar{u}^{j+},\bar{u}^{j-}) = \\ &\frac{1}{2}\left(F(\bar{u}^{j+}) + F(\bar{u}^{j-})\right) - \frac{1}{2}\beta\,\lambda_{\max}\left[\bar{u}^{j+} - \bar{u}^{j-}\right],\end{aligned} \tag{3.12}$$

where F is again the outward pointing normal flux component at an interface, β is a real number which allows control over the amount of numerical viscosity (with $\beta = 1$ being the classical LF definition) and $\lambda_{\max}$ corresponds to the maximum eigenvalue of the Euler flux matrix as

$$\lambda_{\max} := \max_{\bar{u}^{j+},\bar{u}^{j-}}(|\vec{v}| + c), \tag{3.13}$$

Here, c denotes the speed of sound waves computed as $c := \sqrt{\kappa RT}$. For the local LF variant considered in this work, the value of $\lambda_{\max}$ is computed from the local flow field. It should be noted that this flux formulation displays the structure of a central flux combined with a D matrix term, so the dissipation matrix D^1 is

$$D^1[\bar{u}] = D^1(\bar{u}^{j+},\bar{u}^{j-}) = -\frac{1}{2}\beta\,\lambda_{\max}\left[\bar{u}^{j+} - \bar{u}^{j-}\right]. \tag{3.14}$$

Roe's approximate Riemann solver

For the approximate Riemann solver due to Roe, the exact flux Jacobian $A = \frac{dF}{du}$ is replaced by a linearisation $\tilde{A}$ about an average *Roe state*. The underlying system becomes linear with constant coefficients, i.e. instead of the exact Riemann problem, an approximation is generated, which is then solved *exactly*. The numerical flux is approximated as

$$g^2(\bar{u}^{j+},\bar{u}^{j-}) = \frac{1}{2}\left(F(\bar{u}^{j+}) + F(\bar{u}^{j-})\right) - \frac{1}{2}\beta\sum_{i=1}^{m}\tilde{\alpha}_i|\tilde{\lambda}_i|R^{(i)}, \tag{3.15}$$

where the $\tilde{}$ denotes the evaluation at the Roe state, m stands for number of eigenvalues $\lambda_i(\bar{u}^{j+},\bar{u}^{j-})$ of $\tilde{A}$, $\tilde{\alpha}_i(\bar{u}^{j+},\bar{u}^{j-})$ denote the wave strengths and $R^{(i)}$ are the corresponding right eigenvectors. There are two different approaches to find the intermediate state and from there the wave strengths and eigenvectors, which are detailed in Toro (1999). In our approach, we use the classical Roe formulation. The associated dissipation matrix D^2 is given by

$$D^2[\bar{u}] = D^2(\bar{u}^{j+},\bar{u}^{j-}) = -\frac{1}{2}\beta\sum_{i=1}^{m}\tilde{\alpha}_i|\tilde{\lambda}_i|R^{(i)}, \tag{3.16}$$

Returning to Equation (3.7), the right hand side is thus a function of grid resolved quantities $\bar{u}$, which serve as input parameters for the model determined by $\mathbf{B}, \mathbf{K}$ and γ. The target quantity ΔF is computed as the difference between the exact fluxes based on the fully

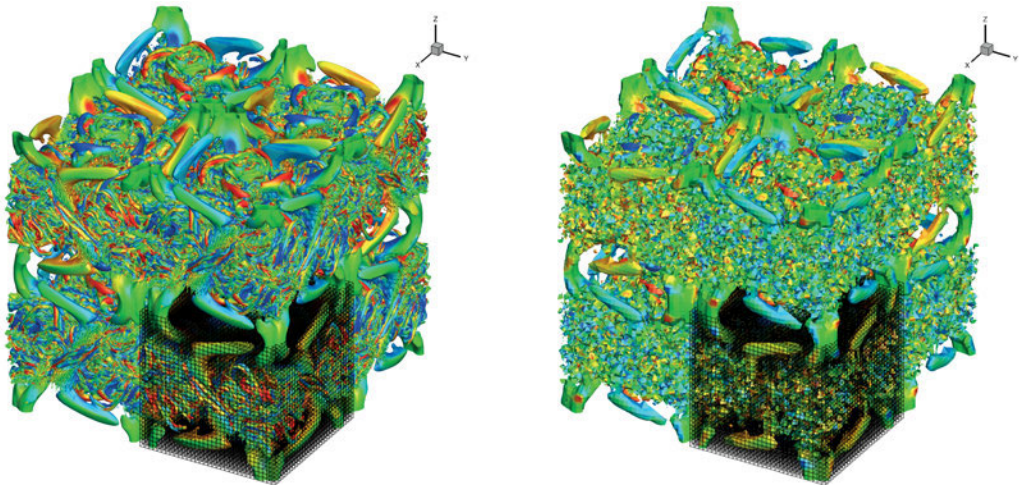

Figure 5: Taylor-Green vortex at $t = 10$, *left:* DNS solution, *right:* Finite Volume reconstruction. (Contours of $\lambda_2 = -0.1$, coloured by relative helicity).

resolved flow field and their central evaluation based on $\bar{u}$. For this approach, a hybrid high order Discontinuous Galerkin-Finite Volume framework was developed, which allows the highly efficient and parallel generation of both the DNS and coarse grid data for the model training. Details of this framework and its implemenation can be found in Appendix B.

Due to the symmetries of this flow problem detailed in section 3.2.1, it is sufficient to analyse only one eighth of the cubic domain, i.e. an equi-sided box of length π. The full domain is depicted in Fig. 5, with an eighth of the computational grid and the associated analysis box shown in the frontal lower right quadrant. Since our framework includes a parallel implementation of the Discontinuous Galerkin Spectral Element Method and a Finite Volume based discretization, these schemes both share this same grid, and the collecting of the FV coarse grid data occurs during the DNS run. In Fig. 5, the left subplot shows a time snapshot of the high resolution solution, while the right subplot depicts the associated second order FV reconstruction on the common grid.

The high order simulations were run on a grid with 64^3 elements, each of which contains a 6th-order tensor product polynomial representation of the solution, leading to a total of about 57 mio degrees of freedom. The simulation was run from $t = 0$ to $t = 15$, and samples for the FEM-BV-VX were taken at an interval of 0.00025, resulting in a time series of length 60000. Within the analysis region shown in Fig 5, 8^3 equispaced cells C^j, $j = 1 \ldots 512$, where flagged as analysis cells. The analysis region is discretized by 32^3 cells, so within this region, the distribution of the 8^3 analysis cells is given by the grid spanned by $(i, j, k) \in [2\ 6\ 10\ 14\ 18\ 22\ 26\ 30]^3$, where (i, j, k) denotes the cell index in the three coordinate directions. It should be noted that no analysis cell is located directly at the boundaries of the domain, due to the need for efficient linear reconstruction based on the neighbouring values, and that the distribution of the cells is not strictly symmetrical about the centre of the analysis box.

Table 2: Parameters of the specific cases *A* and *B*, *CG* as coarse grid.

Case	CG resolution	No of snapshots	No of cells
A	$25 \times 25 \times 25$	16	15625
B	$50 \times 50 \times 50$	33	125000

Within each analysis cell j, we consider only the fluxes across those faces where the outward pointing normal vector is aligned with the associated Cartesian coordinate axis, i.e. the x^+, y^+ and z^+ sides of the cell.

4 Model fitting results

4.1 Turbulent channel flow

We now present the FEM-BV-VX data analysis of the flux correction data for the turbulent channel flow test case. We focus on two particular coarse grid resolutions, hereafter referred to as case *A* and case *B*, and the coarse grid in case *B* has a finer resolution that is twice as in case *A*. Table 2 shows the parameters for both cases. We will first address to case *A* and will present the results of case *B* afterwards.

Before doing the FEM-BV-VX analysis, the computations of the fluxes are checked for consistency. Particularly, a boundary cell has one cell face that represents the (rigid) channel wall. At the wall face, the advection part of the fluxes across the boundary should be zero. In contrast, that flux should be non-zero at the opposite cell face which is aligned towards the channel interior. We found that the calculated time series of the exact flux at these two cell faces confirm the just mentioned feature (we waive a figure's presentation here).

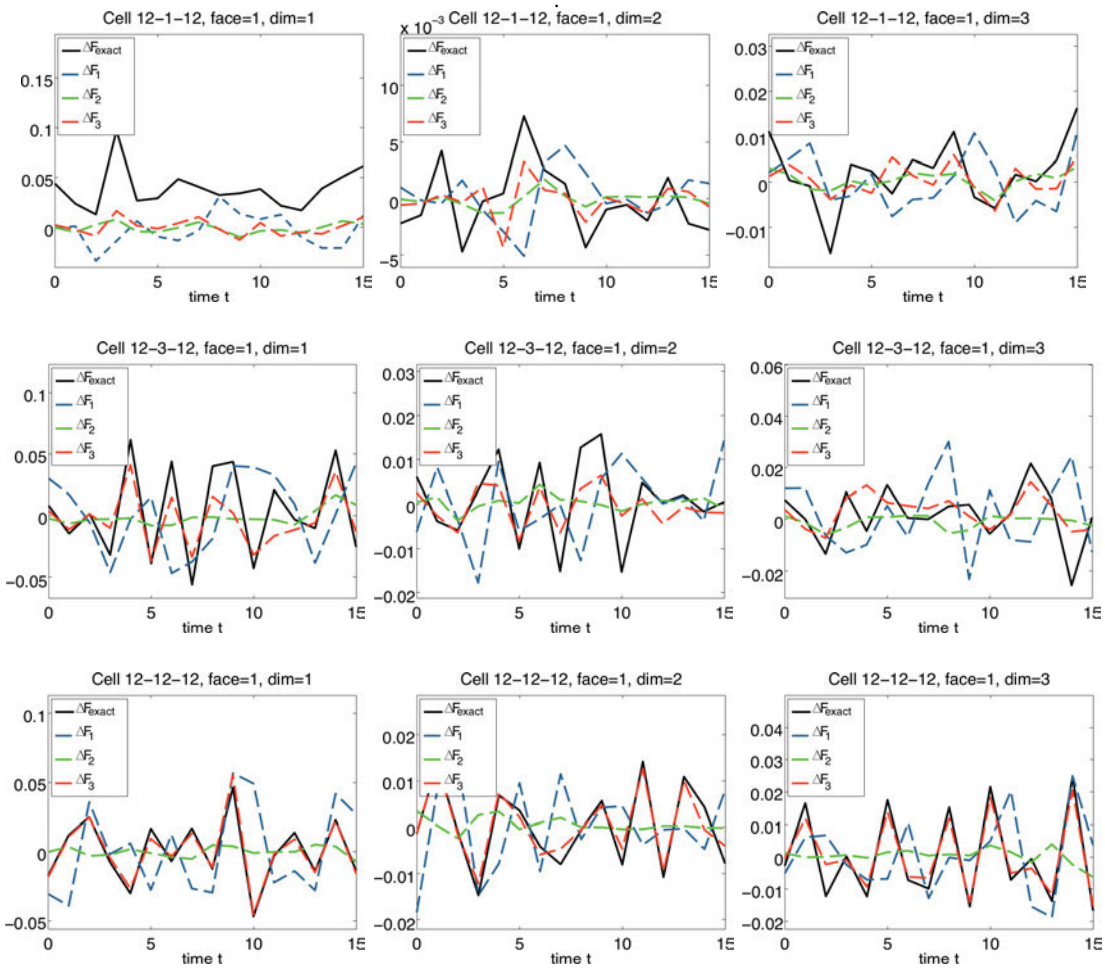

Figure 6: Case *A*: exact flux corrections and numerical flux corrections for face 1 of three specific grid cells. *Upper row*: boundary cell (index 12-1-12), *middle row*: near-boundary cell (index 12-3-12), *lower row*: cell located in the centre of the channel (index 12-12-12). *From left to right*: *x*-, *y*-, *z*-component of the normal vector of the individual flux correction term. Note the different scaling of each figure.

For the discussion in the following sections it appears worth reminding the reader that each grid cell consists of 6 cell faces, and each flux correction term has 3 normal vector components at each face, resp. For each cell j and each face $a = 1, \ldots, 6$, the specific fluxes are calculated as described in Appendix A and time series of the following LES observables are calculated:

- exact flux correction $\Delta F^{j,a}_{\text{exact}}(t) \in \mathbb{R}^3$,
- 1st order flux correction $\Delta F^{j,a}_{1}(t) \in \mathbb{R}^3$,
- 2nd order flux correction $\Delta F^{j,a}_{2}(t) \in \mathbb{R}^3$,
- 3rd order flux correction $\Delta F^{j,a}_{3}(t) \in \mathbb{R}^3$,
- Velocity field $\vec{V}^j(t) \in \mathbb{R}^{21}$ consisting of the average velocity field of cell j and of the average velocity fields of all cells sharing a common face with j. Formally, $\vec{V}^j(t)$ has the form

$$\vec{V}^j(t) = \Big(\vec{v}^{j,0}(t), \vec{v}^{j,x+}(t), \vec{v}^{j,x-}(t), \vec{v}^{j,y+}(t), \vec{v}^{j,y-}(t), \vec{v}^{j,z+}(t), \vec{v}^{j,z-}(t)\Big) \in \mathbb{R}^{21}, \quad (4.1)$$

where the second superscript index indicates the relative position of the neighbour cells with respect to grid cell j under consideration.

Thus, the dimension of the flux correction terms per cell is

$$\Delta F^j_i(t) = \Big(\Delta F^{j,1}_i(t), \ldots, \Delta F^{j,6}_i(t)\Big) \in \mathbb{R}^{18}, i = 1, \ldots, 3, \quad (4.2)$$

and so (3.1) is of dimension

$$\mathbf{B}\phi_2(u) = \Big(\Delta F^j_1(t), \Delta F^j_2(t), \Delta F^j_3(t), V^j(t)\Big) \in \mathbb{R}^{18+18+18+21} \quad (4.3)$$

per cell. Note, that the total number of model parameters is 76 as the additive parameter μ is considered, too (cf. (2.4)).

We focus on face 1 and consider three particular grid cells, that is a boundary cell, a near-boundary cell, and a cell located in the centre of the channel. Note, that cell face 1 is normal to the main flow direction. Fig. 6 shows time series of the exact flux corrections $\Delta F_{\text{exact}}(t)$ and of the numerical flux corrections $\Delta F_1(t), \Delta F_2(t)$ and $\Delta F_3(t)$. In the figure, each row shows subfigures of the respective normal vector component of the different flux corrections.

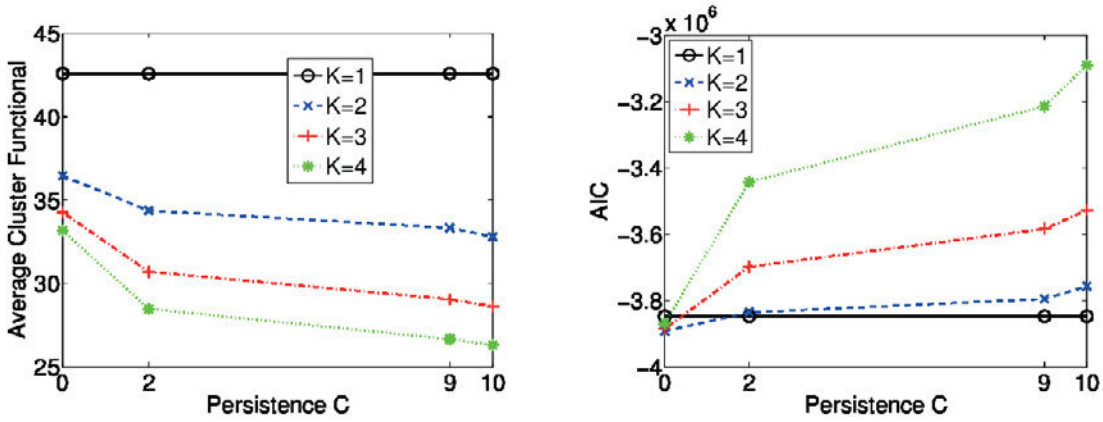

Figure 7: Case *A*: average cluster functional (left panel) and mAIC (right panel) as a function of the number of local models **K** and of the persistence bound **C**. Note, that the computations were limited to $\mathbf{K}_{\max} = 4$, $\mathbf{C}_{\max} = 10$. The optimal parameters are $\mathbf{K} = 2$ and $\mathbf{C} = 0$ as the mAIC has its minimum there.

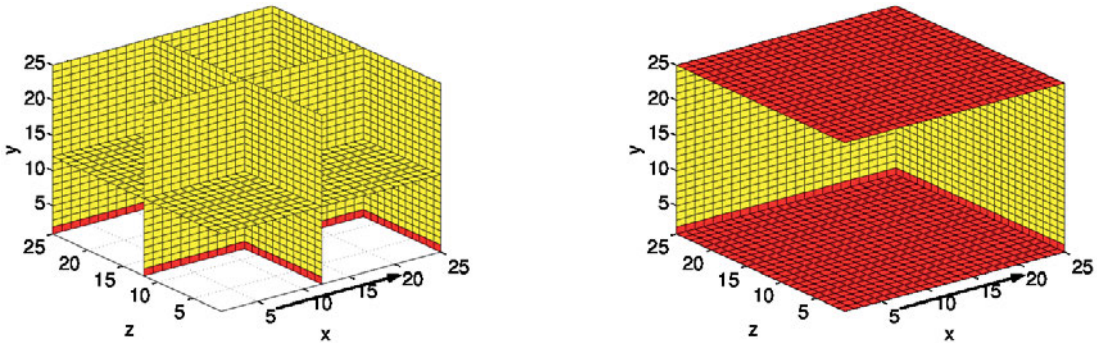

Figure 8: Case *A*: local models (cells' cluster affiliations) based on the optimal ($\mathbf{K} = 2, \mathbf{C} = 0$)-VX-solution. *Wall model* coloured red, *core model* coloured yellow. The arrow indicates the main flow direction.

In all panels, some mismatch is observed between the 1st- and 2nd-order numerical flux corrections, and good agreement between the exact flux correction and the third order flux correction is especially given for all components of the centred cell and of the near-boundary cell. As observed for ΔF_1 and for ΔF_2, some deviations are found also for the third order flux correction term in all components of the boundary cell.

We now look for the optimal model that best-fit the time series of the exact flux correction terms. As described in Section 2.1 the optimal model is linked with a minimum of the mAIC given the number of local models, **K**, and persistence, **C**. For case *A*, the analysis of the mAIC (Fig. 7, right panel) shows a minimum at $\mathbf{K} = 2, \mathbf{C} = 0$. Even if those mAIC-optimal parameters do not result in an absolute minimum of the average cluster functional, **L**, (Fig. 7, left panel), we conclude that the optimal model parameters result in a stationary case ($\mathbf{C} = 0$) and two local models ($\mathbf{K} = 2$) distributed among the individual grid cells.

As shown in Fig. 8, one of these local models is linked with the boundary cells located at the (rigid) channel walls and on the other hand the flow interior is represented by the second local model. This separation in wall flow and interior flow holds for the channel domain in total. For obvious reasons, we name the two different local models *wall model* and *core model*.

Moreover, as indicated by $\mathbf{C} = 0$, we found no time-dependence but stationarity, i.e. there is no switch between those two local models in time, and one and only one of the two local models is assigned to the individual cells.

With the two local models at hand, we now analyze the best-fit model of the time series of the exact flux corrections per cell. Modelling the exact flux correction terms with the best-fit parameters results in the *fitted* flux correction term, ΔF_{fitted}, and Fig. 9 shows the results of those fitted flux corrections for the same cells as presented in Fig. 6. The time series of the fitted flux correction and of the exact flux correction agree well, apart from minor deviations, and particularly good agreement is given in all components of the channel centre cell (lower row in Fig. 9). Note, that in the boundary cell, the time series of the fitted flux correction term has been constructed with the use of the wall model, and the core model has been used for computing the fitted flux correction time series in the near-wall cell as well as in the centre cell, according to Fig. 8.

We now summarize the analysis of case *B*, which consists of a coarse grid with 50^3 grid cells. We, again,

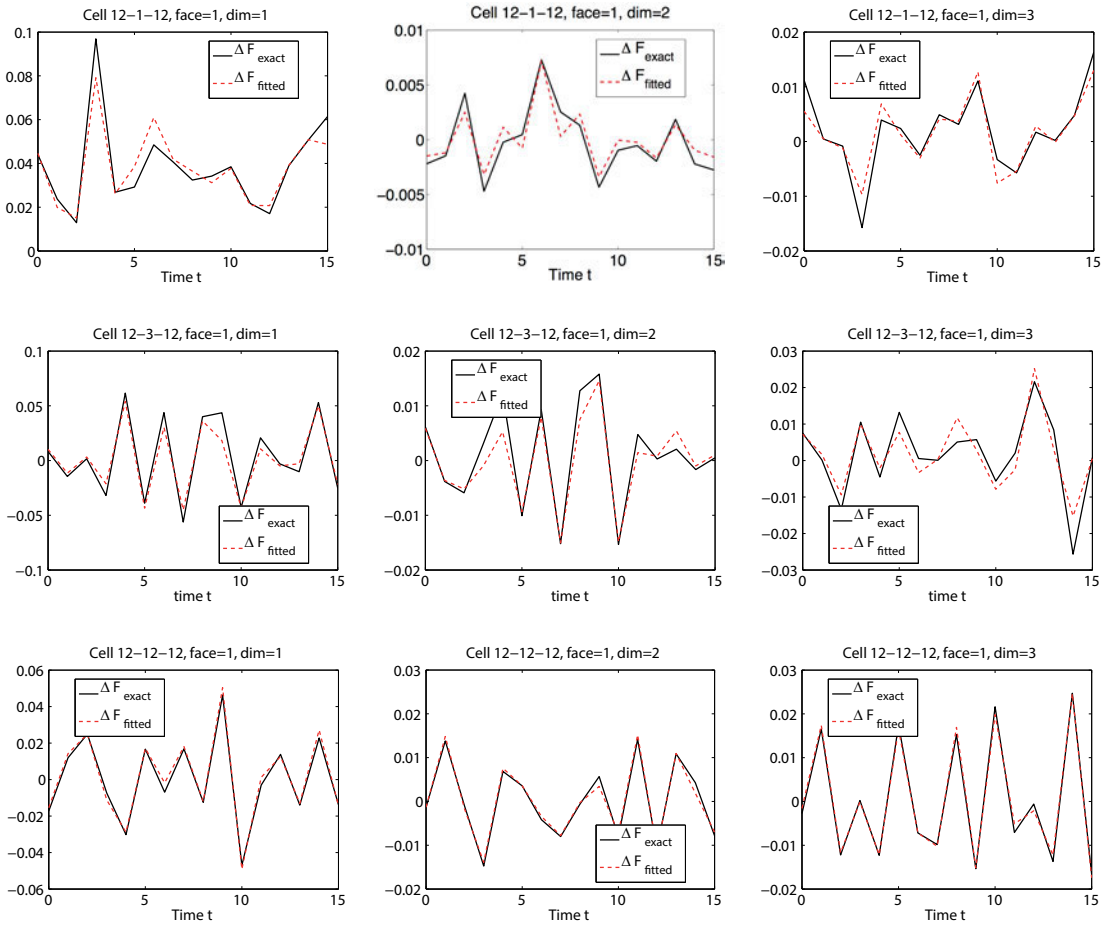

Figure 9: Case *A*: exact flux correction, ΔF_{exact}, vs. flux correction term, ΔF_{fitted}, obtained from the mixture model using the optimal parameter, $(\mathbf{K} = 2, \mathbf{C} = 0)$-VX-solution. Panels show the same cells and the same cell face as in Fig. 6.

determine at first the optimal reconstruction parameters (cf. Fig. 10). Now, the minimum of the mAIC is found at $\mathbf{K} = 3, \mathbf{C} = 0$, i.e. the optimal model-fit parameters result in a stationary model as in case *A*, but in contrast three different fluctuation regimes are obtained here. Regarding the distribution of the local models among the individual cells, as shown in Fig. 11, two of them are assigned to wall cells and cells in the channel interior as in case *A*, therefore again called *wall model* and *core model*, and the third regime, hereafter called *transition model*, is mainly assigned to cells which are located close to the wall cells.

Considering the approximation of the exact flux correction term, i.e. the model-fit, see Fig. 12, the time series of the fitted flux correction term agrees well with the exact flux correction at channel centered cells, and only minor differences are observed at boundary cells as well as at near-boundary cells. Furthermore, the best-fit model represents the exact flux correction data more accurate than it does in case *A* particularly at the boundary and at the near-boundary cell.

In the next section, the results of the Taylor-Green vortex flow test case will be presented. The results presented in this section for the turbulent channel flow test case will then be discussed in Section 5.1.

4.2 Taylor-Green vortex flow

In this section, we present the results of the data analysis framework described in Section 2 and 3.2 applied to the Taylor-Green vortex flow. For each of the 8^3 analysis cells j the time series $t = 0 \ldots 59999$ of the following LES-observables is gathered and made available to the FEM-BV-VX analysis tool chain:

- the flux corrections with respect to the Finite Volume central flux, containing the three momentum fluxes across the x^+, y^+ and z^+ sides, $\Delta F = F_{\text{ex}}(u) - F_{\text{central}}(\bar{u}) \in \mathbb{R}^9$,
- the Lax-Friedrichs dissipation terms $R_1^j(t) = F_{\text{central}}(\bar{u}) - F_{LF}(\bar{u}^{j+}, \bar{u}^{j-}) = F_{\text{central}}(\bar{u}) - g^1(\bar{u}^{j+}, \bar{u}^{j-}) \in \mathbb{R}^9$
- the Roe dissipation terms $R_2^j(t) = F_{\text{central}}(\bar{u}) - F_{\text{Roe}}(\bar{u}^{j+}, \bar{u}^{j-}) = F_{\text{central}}(\bar{u}) - g^2(\bar{u}^{j+}, \bar{u}^{j-}) \in \mathbb{R}^9$
- the Smagorinsky dissipation term $R_3^j(t) = F_{\text{SGS}} \in \mathbb{R}^9$
- the mean velocity components $V^j(t) = (u(t), v(t), w(t))^j \in \mathbb{R}^{21}$ of the analysis cell j and its direct neighbours, i.e. the six surrounding cells sharing a common face with cell j.

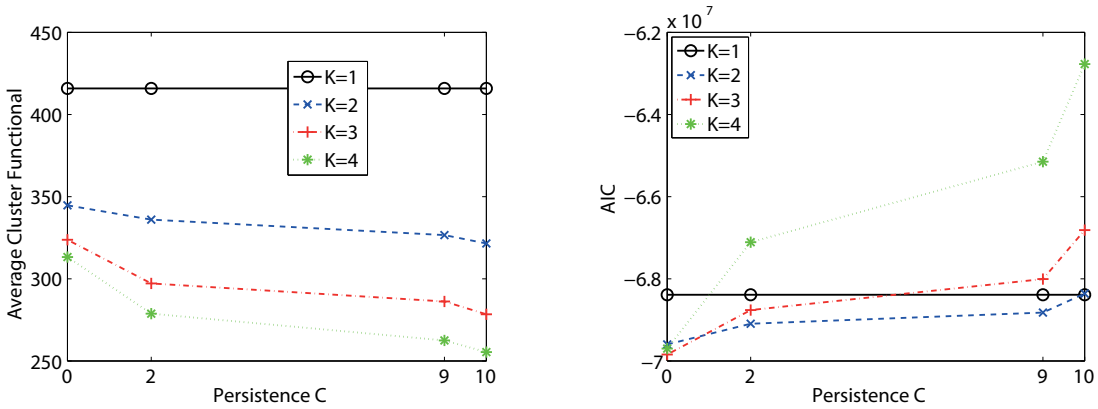

Figure 10: as in Fig. 7 but for case *B*. The optimal parameters are $\mathbf{K} = 3$ and $\mathbf{C} = 0$.

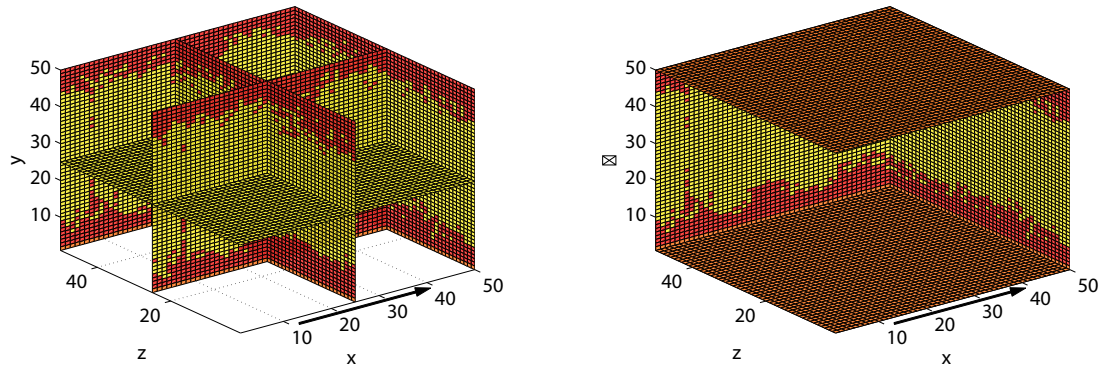

Figure 11: as in Fig. 8 but for case *B*, i.e. the optimal $(\mathbf{K} = 3, \mathbf{C} = 0)$-VX-solution. *Wall model* coloured brown, *transition model* red, and *core model* coloured yellow.

We fitted the parameters of the non-stationary and non-homogeneous VX-mixture model defined in 3.2

$$\begin{aligned}\Delta F(u^j(t)) =& F_{\text{ex}}(u^j(t)) - F_{\text{central}}(\bar{u}^j(t)) \\ =& \sum_{i=1}^{\mathbf{K}} \gamma_i^j(t) \left(\mu_i(t) + \mathbf{B}_i(\phi_2(\bar{u}^j(t)))\right), \end{aligned} \tag{4.4}$$

where the time series $\bar{u}^j(t)$ of external factors is composed as

$$\bar{u}^j(t) = \left(R_1^j(t), R_2^j(t), R_3^j(t), V^j(t)\right) \in \mathbb{R}^{9+9+9+21}. \tag{4.5}$$

The involved model parameters are consistently sized. For instance, applying the second order data manipulation ϕ_2 function defined in (2.5) results in $\mu_i \in \mathbb{R}^9, \mathbf{B}_i \in \mathbb{R}^{9\times 1224}$, $i = 1, \ldots, \mathbf{K}$.

In Fig. 13, the flux correction and the associated dissipation terms for the x-momentum flux across the x^+ cell face are shown exemplarily for an arbitrary analysis cell over the simulation time. In accordance with the temporal development of the flow as described in Section 3.2, the magnitude of flux correction ΔF remains very small throughout the initial laminar and transitional phase, as the coarse grid Finite Volume discretization is capable of resolving the occurring flow features adequately, and so $F_{\text{ex}}(u) \approx F_{\text{central}}(\bar{u})$. It should however be noted that the flux correction is not trivially zero, so a non-trivial model exists in this region. As a side note, even in this laminar region, the flux $R_3(t)$ is non-zero due to the well-known deficit of Smagorinsky's model in this situation. During the breakdown of the initial vortices of the flow and the build-up of the scale cascade, the turbulent flow can no longer be represented on the coarse grid, and thus the flux correction becomes significant. It shows a strong dynamic in the region between $t = 7$ and $t = 13$, where the scale energy transfer dominates the flow. Due to the dissipative effects at later times, the fluctuations are damped, which in turn results in a reduction of the flux correction terms during that period. The dissipation fluxes R_1, R_2 are very similar and show a high dynamic, while Smagorinsky term R_3 exhibits less fluctuations. This is not surprising, as the flux function based dissipation terms (R_1, R_2) are directly related to the difference in resolution between the exact flow and its coarse grid approximation through the magnitude of the jump term, while the Smagorinsky term R_3 is only governed by the reconstructed coarse grid velocity gradients.

As supported by Fig. 13, the dynamics of the flow mandate a sufficiently high temporal sampling rate to capture the high frequencies accurately. Due to the explicit time integration of our framework, samples are taken at intervals of $t = 0.00025$, a frequency well above the one related to the theoretical limit of the smallest eddies characterized by the Kolmogorov length. Due to

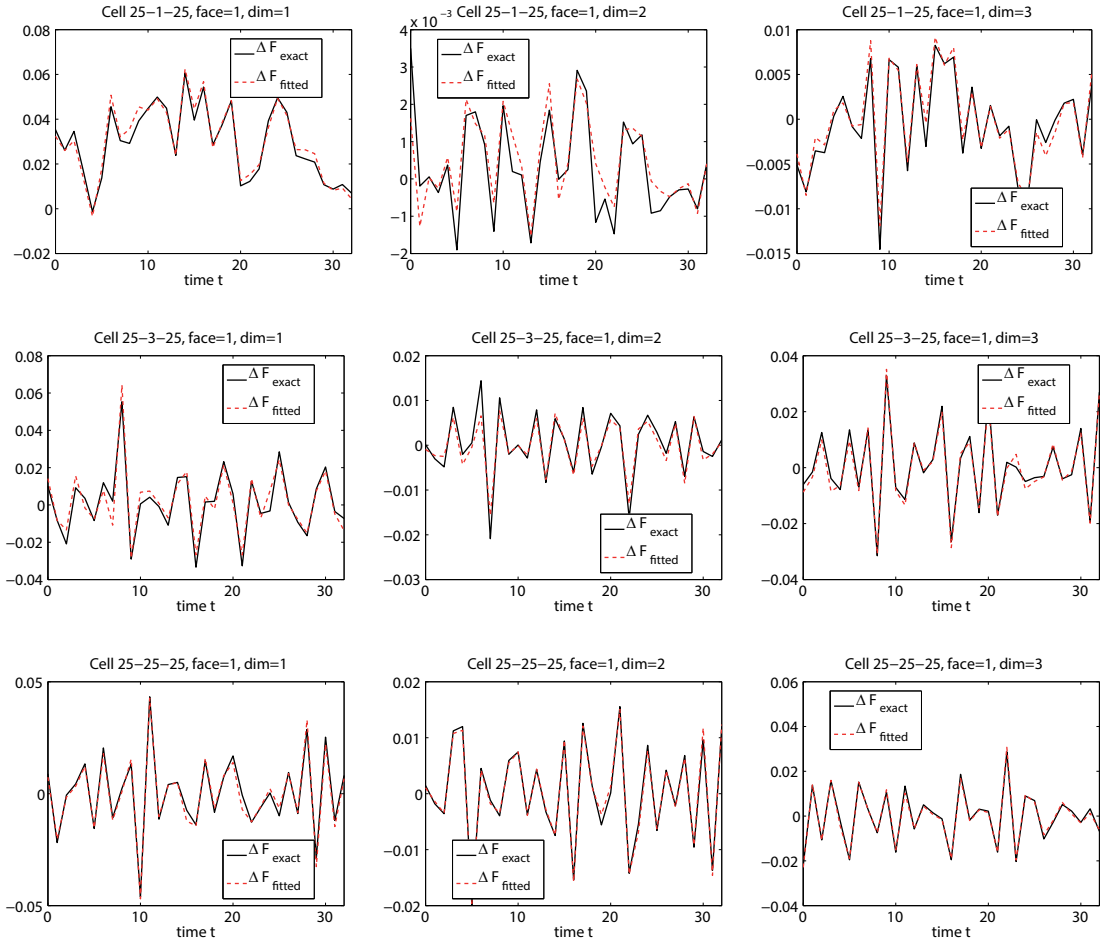

Figure 12: as in Fig. 9 but for case *B*, i.e. optimal ($\mathbf{K} = 3, \mathbf{C} = 0$)-VX-solution. *Upper row*: boundary cell (index 25-1-25), *middle row*: near-boundary cell (index 25-3-25), *lower row*: cell located in the centre of the channel (index 25-25-25).

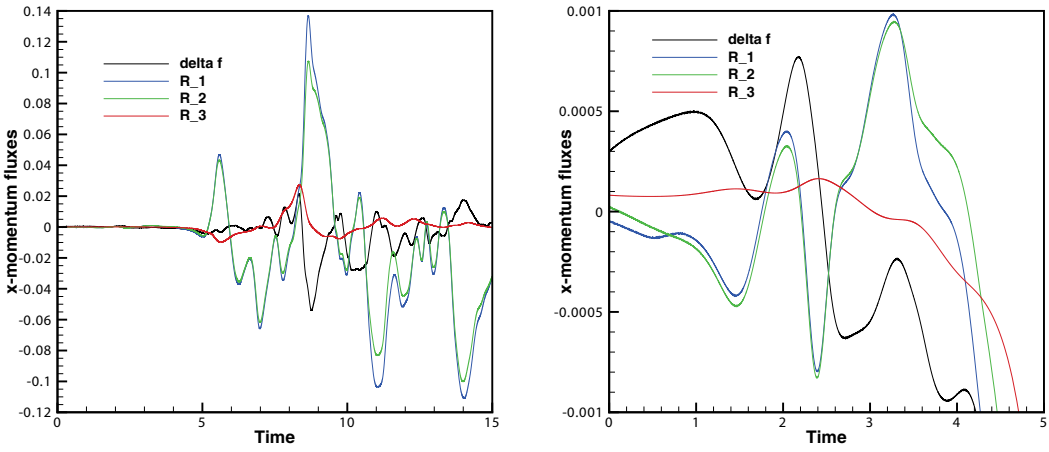

Figure 13: Taylor-Green vortex data: Flux correction and modelling terms for analysis cell 10-10-18. $\Delta F = F_{\mathrm{ex}}(u) - F_{\mathrm{central}}(\bar{u})$, R_1 : Lax-Friedrichs Dissipation, R_2 : Roe Dissipation, R_3 : Smagorinsky-flux *left:* Full time series, *right:* Zoom on transitional regime

the limitations of computational resources, we could not analyse the whole time series and thus sub-sampled it by considering only, e.g., every 200th datum resulting in a time series of length $L = 300$. To study the effect of this sub-sampling, we additionally analysed sub-sampled time series of length $L = 600$ (every 100th datum) and of length $L = 1200$ (every 50th datum).

Fig. 14 shows the results of our analysis with the FEM-BV-VX approach in terms of the Bayesian information criterion as a function of the sampling length L.

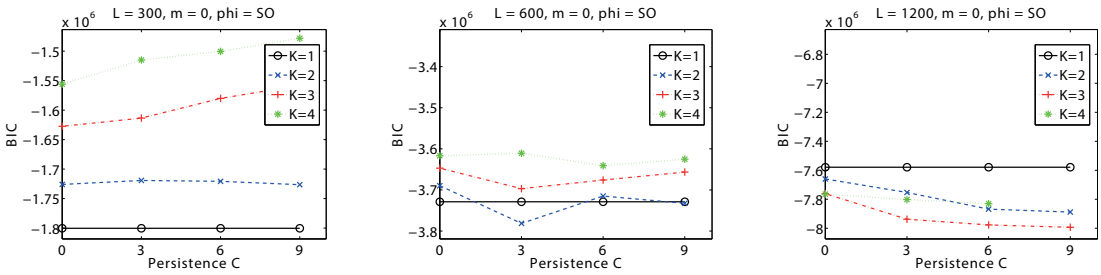

Figure 14: Taylor-Green vortex data: The Bayesian information criterion as a function of the number of clusters $K \in \{1, 2, 3, 4\}$, the upper bound for the persistence $C \in \{0, 3, 6, 9\}$, the memory depth $m = 0$, and the time series length $L \in \{300, 600, 1200\}$.

Table 3: For fixed time series length L, the minimum of the Bayesian information criterion as a function of the memory depth m and the data manipulator function $\phi(\cdot)$ is attained in $m^* = 0$ and $\phi^*(\cdot)$ =**S**econd-**O**rder function. The respective optimal value for the number of clusters K and the persistence bound C is given in the table.

$L = 300$	$L = 600$	$L = 1200$
$(\mathbf{K}^* = 1, \mathbf{C}^* = 0)$	$(\mathbf{K}^* = 2, \mathbf{C}^* = 3)$	$(\mathbf{K}^* = 3, \mathbf{C}^* = 9)$

The number of possible clusters K was set to 4, and the number of allowed temporal model changes (persistence C) was limited by 9. Table 3 lists the optimal parameter set for each L.

It is remarkable that as opposed to the channel flow discussed above, a persistence $C > 0$ is found to be optimal, i.e. the optimal fit to the given data requires a temporal switching of the cell-local model cluster. While this is to be expected from a physical standpoint, it is remarkable that the modelling approach is capable of adapting to the temporal change of solution structure. Figs. 15 and 16 show the results of the optimal fitted model for $L = 1200$ for all 9 flux correction terms for two arbitrarily chosen analysis cells. The first cell (Fig. 15) is located close to the centre of the vortex core. The 9 flux components are of comparable magnitude, which is consistent with the assumption of spatial isotropy in this region. There is also a general pairwise similarity between the y-momentum and z-momentum components on the x^+ face, and the the x-momentum and y-momentum components on the z^+ face, which can also be an indication of isotropy. In general, for this analysis cell, the match between the exact flux correction and its fitted counterpart is excellent.

For the second cell (Fig. 16), which is located close to the periodic boundary of the flow, where the anisotropic large scale structures persist, the fit quality is less satisfactory. A number of high frequency fluctuations in the exact flux correction are visible, which cannot be captured by the fit. The off-diagonal components generally show an inferior agreement, this is however most likely due to the small amplitude of the exact flux corrections themselves.

In Fig. 17, the cluster affiliations of two typical cells over time are shown again for the optimal fit for $L = 1200$. Cell 236 is located again in the centre of the vortex, while cell 241 is close to the periodic boundary. For both cells, cluster 2 is active for the well-resolved initial laminar period, and both cells return to this model at the end of the observed time period, where the dissipation action dominates. For cell 241 close to the boundary, this model remains active almost all the time, which can be explained by the prevalence of the large scale structures in this region. Cell 236 shows a stable model change from model 2 to 3 at around $t = 7$, the time when the turbulent scale spectrum begins to develop, leading to severe under-resolution of the structures by the coarse grid and thus the need for a different closure model. It is remarkable that right when the solution changes is characteristics from an ordered, small bandwidth state to a chaotic, high bandwidth situation, the FEM-BV-VX detects the need for a change in fitting strategy. Supporting this observation is the fact that a return to the (laminar) model 2 occurs in the later stages of dissipative decay (at around $t = 13$), when the representation on the coarse grid becomes smoother again.

Figs. 18 and 19 put these two cells into their spatial context. In these plots, the cluster affiliations of 8×8 analysis cells on a $z = const.$ slice through the analysis box are shown. The approximate centre of the vortex core is marked, and it should be noted that due to the location of the analysis cells, the outer layer of cells is not directly located at the periodic boundaries. As observed before, initially, model 2 is appropriate for all cells during the laminar phase. With the onset of transition, model switches occur for the inner cells. After the peak of the turbulent scale production, all but the inner cells return to the initial model.

5 Discussion

5.1 Turbulent channel flow

In Section 4.1, we have presented the results of the modelling approach of the fully turbulent channel flow data. Two cases with particular coarse grid resolution, denoted as case A, with $25 \times 25 \times 25$ cells in (x, y, z) and

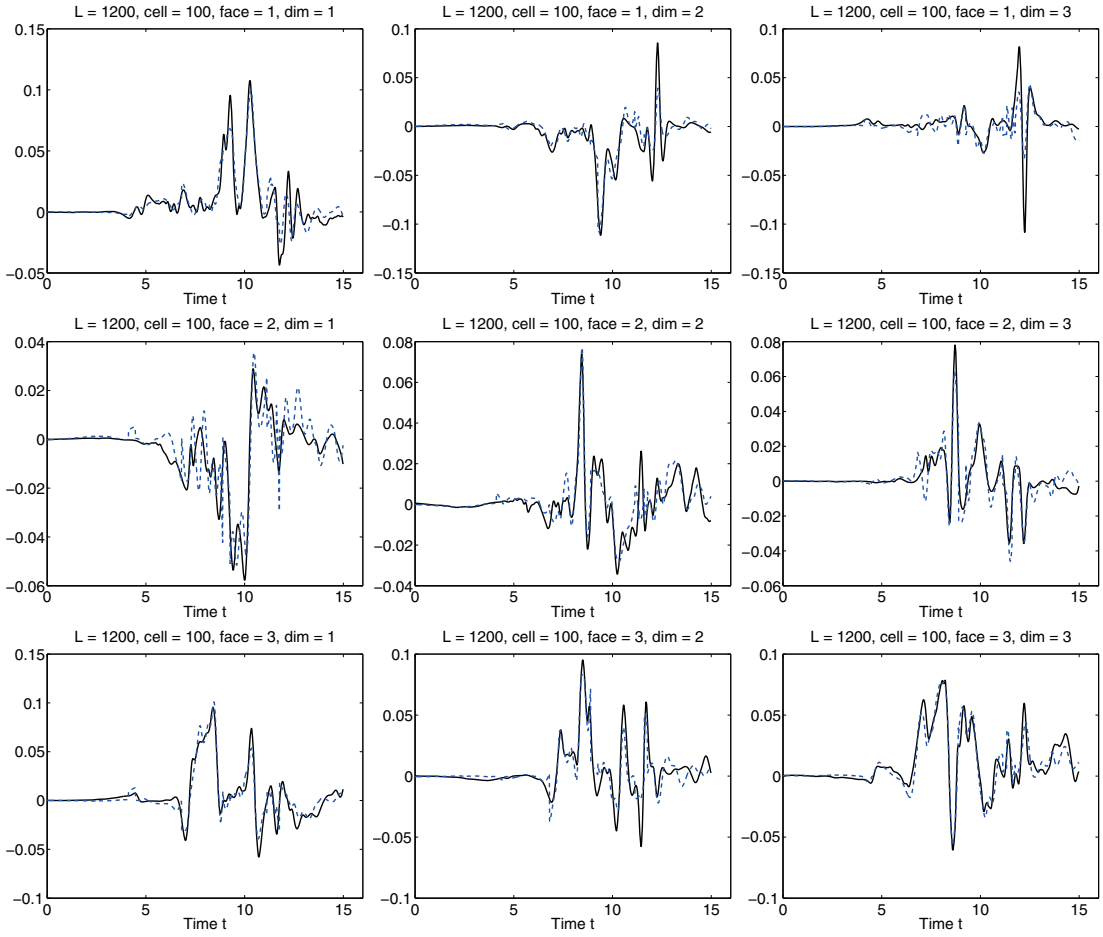

Figure 15: Taylor-Green vortex data: Exact corrections ΔF vs. fitted corrections. Results for the (optimal) non-stationary and non-homogeneous ($\mathbf{K}^* = 3, \mathbf{C}^* = 9$)-VX-solution with memory depth $m = 0$ and data manipulation function $\phi(\cdot) = SO(\cdot)$ trained on sub-samplings with length $L = 1200$ of the cell 100 time series. Solid black lines: ΔF_{exact}, dashed blue lines: ΔF_{fitted}.

case *B*, with $50\times50\times50$ cells, were applied to the model framework to model the exact flux correction term.

In case *A*, two particular fluctuation regimes, or local models, a *wall model* and a *core model*, are explored by the model framework, and a third fluctuation regime, the *transition model*, has been obtained in case *B*. Thus, we found resolution-dependent closure regimes. Furthermore, even though the data are clearly non-homogeneous, as observed in the model-fit flux correction data, our results show no time-dependence, i.e. the local models captured are stationary models.

Considering the physics of the turbulent channel flow, it is generally accepted that the flow is statistically independent of z (at least away from the end-walls) provided that the extent of the channel in spanwise z-direction is large compared to the wall-normal y-direction. Furthermore, in the fully developed region of turbulent channel flows, the flow being considered is statistically stationary and statistically one-dimensional, with velocity statistics depending on the y-coordinate only.

The (equidistant) grid resolution chosen for case *A* (case *B*) leads to a grid size of $\Delta_y^+ = 47.2$ (23.6) in terms of wall units ($y^+ = \frac{y}{\delta_v}$, with δ_v as viscous lengthscale), whereas the resolution of the auxiliary fine grid, $N_y = 350$ (cf. Fig. 2), leads to $\Delta_y^+ = 3.37$. Considering the various wall regions in the turbulent channel flow (see e.g., Pope (2000) for a detailed description), it follows, therefore, that the viscous wall region, $y^+ < 50$, where the viscous contribution to the shear stress is significant, is resolved with 1 grid cell in case *A* and with 2 grid cells in case *B*, while the viscous sublayer ($y^+ < 5$) is not resolved in both cases. Also the buffer layer is fully immersed within the first cell for case *A* and within two cells for case *B*. However, the viscous wall region must be considered unresolved in case *B*, too, as 2 grid cells are not sufficient to capture the physics of that region. Note, that the viscous wall region would be indeed resolved with the equidistant fine grid but the viscous sublayer would not. However, the original DNS, from which the fine and the coarse grid data were computed, has been performed such that sublayers have been resolved, a Chebyshev-tau formulation in wall normal direction was used for the grid generation.

The results found for the cells' cluster affiliations of both coarse grids support what has been just mentioned. Only two general models were recognized by the model framework for case *A*, while the inner layer and sub-

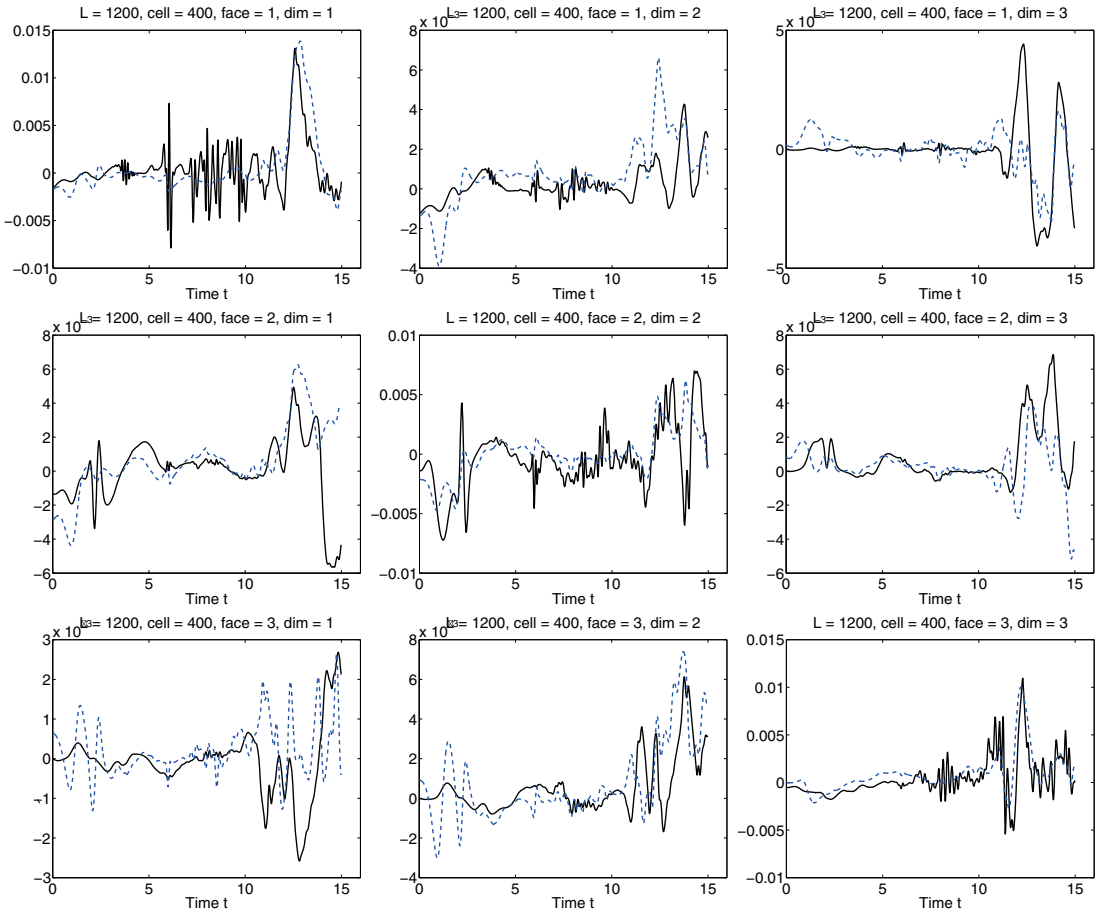

Figure 16: Taylor-Green vortex data: Exact corrections ΔF vs. fitted corrections. Results for the (optimal) non-stationary and non-homogeneous ($\mathbf{K}^* = 3, \mathbf{C}^* = 9$)-VX-solution with memory depth $m = 0$ and data manipulation function $\phi(\cdot) = SO(\cdot)$ trained on sub-samplings with length $L = 1200$ of the cell 400 time series. Solid black lines: ΔF_{exact}, dashed blue lines: ΔF_{fitted}.

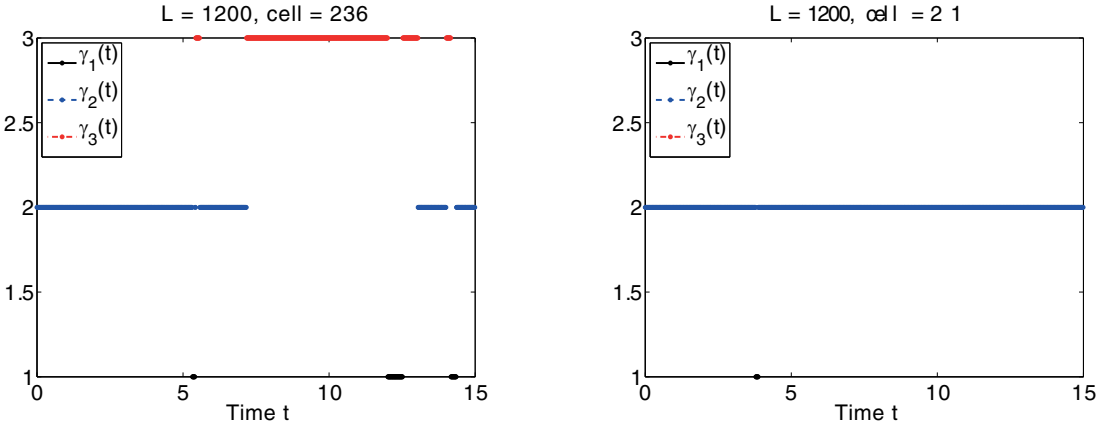

Figure 17: Taylor-Green vortex data: The cluster affiliations for a typical inner (cell no. 236, *left*) and boundary cell (cell no. 241, *right*). Results for the optimal ($\mathbf{K}^* = 3, \mathbf{C}^* = 9$)-VX-solution of sub-sampling length $L = 1200$.

layers of the overall inner and outer wall region could not be resolved due to the coarse grid size. In that fashion, we interpret the so-called *transition model* observed in case *B* as a model state representing the inner layer which is generally influenced also by the log-law wall region and overlapping with the outer layer. As the inner layer is limited to $y/h < 0.1$ with h as the channel half width (cf. Pope (2000)), it is therefore comprehensible that the transition model is also assigned to some cells that actually appear remote from the endwalls (cf. Fig. 11).

As repeatedly mentioned in Section 2.1, our model ansatz originally incorporates a deterministic-stochastic approach but our analysis revealed that the deterministic

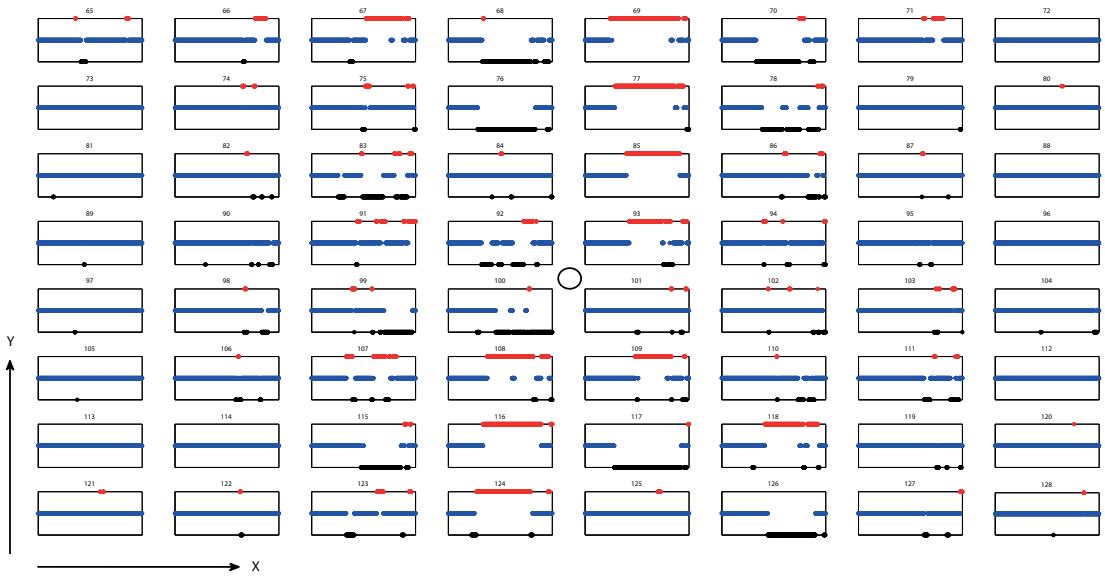

Figure 18: Taylor-Green vortex data: The cluster affiliations for 8×8 analysis cells in the $z = \frac{11}{64}\pi$ plane. The approximate location of the vortex centre is denoted by a circle. Results for the optimal ($\mathbf{K}^* = 3, \mathbf{C}^* = 9$)-VX-solution of sub-sampling length $L = 1200$.

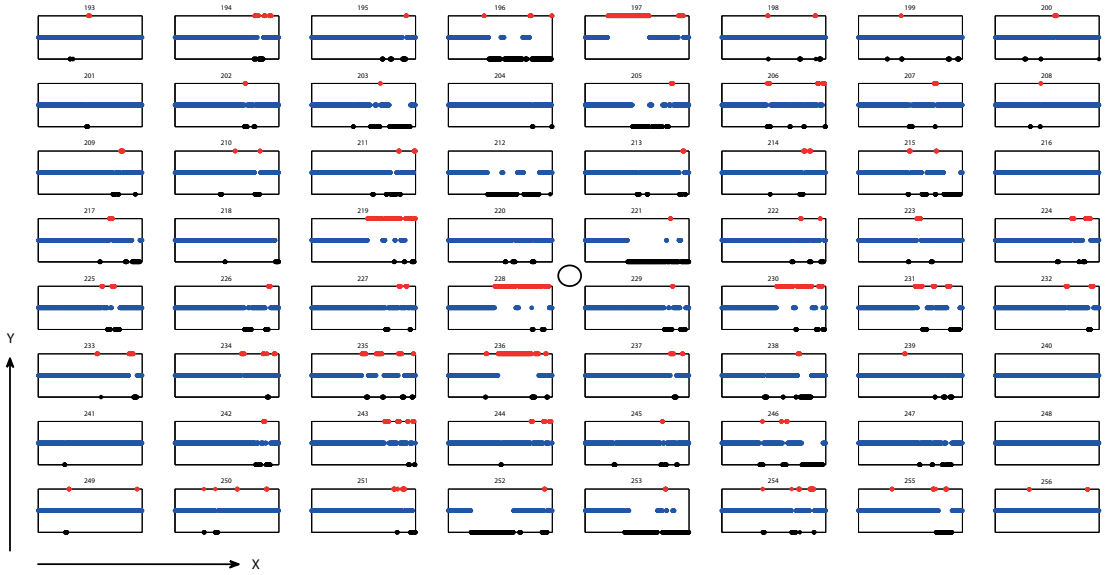

Figure 19: Taylor-Green vortex data: The cluster affiliations for 8×8 analysis cells in the $z = \frac{27}{64}\pi$ plane. The approximate location of the vortex centre is denoted by a circle. Results for the optimal ($\mathbf{K}^* = 3, \mathbf{C}^* = 9$)-VX-solution of sub-sampling length $L = 1200$.

model part alone already yields surprisingly low residuals and the stochastic term, therefore, is not interpreted here. Fig. 9 and Fig. 12 already provide a qualitative visual comparison of flux corrections with their reference values for selected cells and might be provided to guide reader's intuition. Now, we evaluate a quantitative measure using error norms of the residuals as objective criteria. For this purpose, we calculate the local and global type of the Euclidian norm of the residuals and, for the local type, evaluate the local maximum per time series.

The relative and absolute error in the local form of the Euclidian norm reads

$$e_{loc,rel}(t) := \frac{\|\Delta F_{\text{exact}}(t) - \Delta F_{\text{fitted}}(t)\|}{\|\Delta F_{\text{exact}}(t)\|} \tag{5.1}$$

and

$$e_{loc,abs}(t) := \|\Delta F_{\text{exact}}(t) - \Delta F_{\text{fitted}}(t)\|, \tag{5.2}$$

and the error in the global form of the Euclidian norm reads

$$e_{\text{global}} := \sqrt{\sum_t |\Delta F_{\text{exact}} - \Delta F_{\text{fitted}}|^2}. \tag{5.3}$$

In general, when the values of the flux correction terms are small, the relative error should get particular attention, a small absolute error would say little about the quality of the fit. However, values very close to zero

Table 4: Case *A*: relative and absolute local error, and global error of the residuals following (5.1)–(5.3).

Cell (face 1)		$\max(e_{loc,rel}(t))$	$\overline{(e_{loc,rel}(t))}$	$\max(e_{loc,abs}(t))$	e_{global}
	dim=1	0.3203	0.1168	0.0178	0.0280
12-1-12	dim=2	5.8415	0.9101	0.0022	0.0045
	dim=3	1.7936	0.4609	0.0061	0.0107
	dim=1	1.0126	0.3252	0.0254	0.0367
12-3-12	dim=2	1.8322	0.5276	0.0071	0.0110
	dim=3	12.9632	1.9502	0.0104	0.0173
	dim=1	1.4090	0.2297	0.0051	0.0107
12-12-12	dim=2	0.6687	0.1848	0.0024	0.0041
	dim=3	2.5993	0.3327	0.0020	0.0043

Table 5: Case *B*: relative and absolute local error, and global error of the residuals following (5.1)–(5.3).

Cell (face 1)		$\max(e_{loc,rel}(t))$	$\overline{(e_{loc,rel}(t))}$	$\max(e_{loc,abs}(t))$	e_{global}
	dim=1	1.5687	0.1515	0.0063	0.0169
25-1-25	dim=2	53.1293	2.3397	0.0019	0.0036
	dim=3	24.3831	1.3463	0.0027	0.0064
	dim=1	11.9546	1.1447	0.0128	0.0287
25-3-25	dim=2	9.5190	0.7604	0.0078	0.0125
	dim=3	24.3804	1.0117	0.0046	0.0117
	dim=1	9.7811	0.6584	0.0064	0.0130
25-25-25	dim=2	8.7102	0.3631	0.0021	0.0041
	dim=3	1.0350	0.1699	0.0032	0.0064

could result in single peak values of the relative error and in such cases the absolute error should gain importance. We, therefore, consider both type of local errors and additionally calculate the arithmetic mean value of the relative error, $\overline{(e_{loc,rel}(t))}$ that might provide an additional indicator for the relative error.

The results for the different cells and directions (x, y, z) according to the panels in Fig. 9 for case *A* and in Fig. 12 for case *B* are shown in Table 4 and 5, resp. For both cases, values of the maximal absolute local error as well as of the global error are much lower than 1 for all subsets, and the values of the relative error are much larger than 1 for almost all cases. A number of peak values partially much greater than 10 are given in case *B*, just one peak event is observed in case *A*. Those peak values have to be seen in relative terms regarding the mean of the relative error which for each event is significantly lower than its peak indicating that the peak is a single event in the time series of the residuals. That is in line with the global error that remains very much lower than 1 at these datums, too. The analysis of the error norms confirm the previously mentioned statement, that the residuals of the model-fit of the exact flux correction terms are small, and, therefore, justify our strategy of considering the deterministic part of the model approach only.

Finally, we are interested in the properties of the local models. More precisely, we would like to describe the significance of the input parameters that form the different local models, cf. (4.3), i.e. the numerical flux correction terms of different order, $\Delta F_{1,2,3}$, and the averaged velocities, $\vec{V}$. We, here, concentrate on case *A* where two local models, the wall model and the core model, are obtained and pick again cell face 1 which is perpendicular to the main flow (x-) direction of the turbulent flow field. As a reminder, the time series of the best-fit flux correction term, ΔF_{fitted}, according to an individual cell face, cf. Fig. 9, is an outcome of the specific local model associated with that grid cell. However, even if we focus on just one cell face, note that each local model considers the best-fit approximation of the flux correction terms across all 6 faces of all grid cells associated with the local model under consideration.

Considering the core model, Fig. 20 shows a matrix visualizing the contribution of the individual factors to the fitted flux correction. The components of the fitted flux correction term are plotted in the rows (top row, middle row, and bottom row represent the x-, y-, and z-component, resp.), and in the columns, the individual model parameters, i.e. the parameter μ, the numerical flux corrections $\Delta F_{1,2,3}$ and the velocity field, $\vec{V}$, are plotted. For the numerical flux corrections, x_+ and x_- denote the cell faces in upstream and downstream direction of the cell under consideration, j, and y_+ and y_- denote the cell faces in y-direction and z_+ and z_- denote the cell faces in z-direction. Note, that each flux across a specific cell face is subdivided in its spatial (x, y, z) components. Similar, the velocity field, $\vec{V}$, is separated in its components, i.e. the neighboured cells and the cell under consideration itself, and, again, the velocity vector of each cell is subdivided in its spatial components, too. According to (2.4) and (4.3), resp., that results in 76 components of the local model, each accounts for a specific contribution.

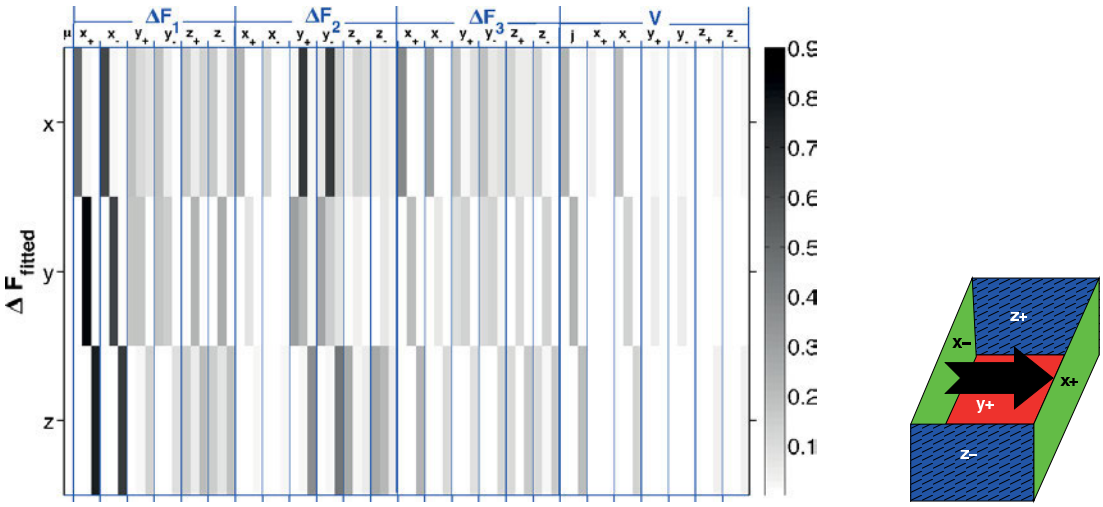

Figure 20: Case A, core model, face 1 (x_+): significance of the model parameters to the fitted flux correction term. Dark color indicates components that contribute much to the fitted flux correction term, components of no importance coloured white. The picture on the right indicates the cell face notation (the arrow denotes the main flow direction).

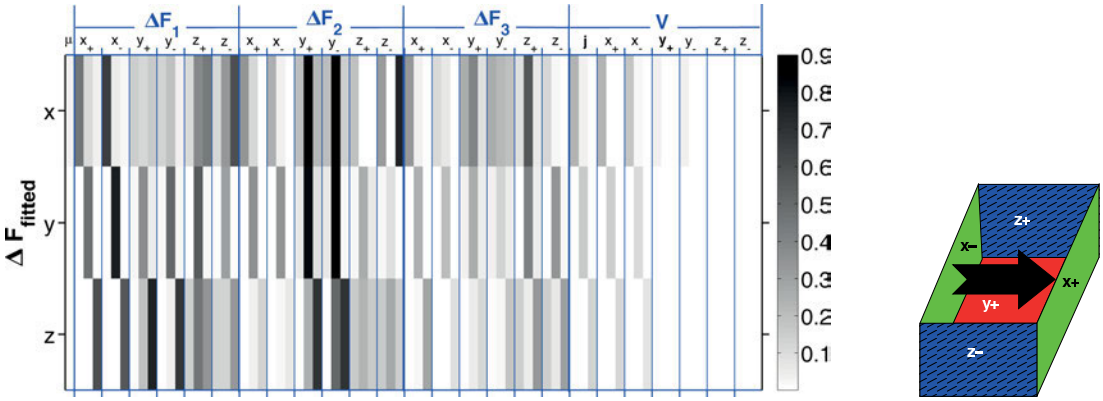

Figure 21: as in Fig. 20 but for the wall model.

To analyze the core model step-by-step, let us, at first, pay attention to the velocity field. It, initially, is conspicuous that the cell under consideration, j, contributes significantly to the local model. Apart from this, only cell x_-, located upstream of the main flow direction, obviously contributes to some extent to that model while cell x_+ as well as the other adjacent cells (those in y- and z-direction) does not. Moreover, only the principal component of the velocity term is of significance for the respective component of the fitted flux correction term, e.g., only the x-component of cell j and x_- contributes to the x-component of ΔF_{fitted}, etc.

Regarding the numerical flux corrections, a number of secondary components of the three different order flux corrections have a part in the local model, coloured grey, and the major contribution comes from the x_+ and x_- cell face of ΔF_1 followed by ΔF_3. In both terms, again, the respective main component is of greatest significance in each case, similar to the findings for the velocity field, which, in total, results in the stripe-shaded look of the picture. A discrepancy is observed regarding the contributions of ΔF_2, where the y-component of the y_+ and of the y_- cell face contributes also with a large amount to the x-component of the fitted flux corrections. It, finally, is noticeable that the model parameter μ is of no significance in all components.

Considering the wall model, Fig. 21, it is, first, interesting to note, even though no real surprise after surveying the core model, that, again, the specific main component of each model parameter dominates the appropriate component of the fitted flux correction term. That is primarily true for the y-component of ΔF_{fitted}, where all model parameters contribute with its y-component only. Again, that results in the stripe-shaded look similar to the core model picture discussed above. As in the core model, the model parameter μ is of no significance in the wall model. Comparing the properties of the velocity field of the core model, here, also the x_+ cell located downstream in the main flow direction now contributes to the wall model.

Comparing both model as such, it is remarkable that the wall and the core model consists of similar features and the major differences between the two models are to a great extend in the x_+ cell of the velocity field as

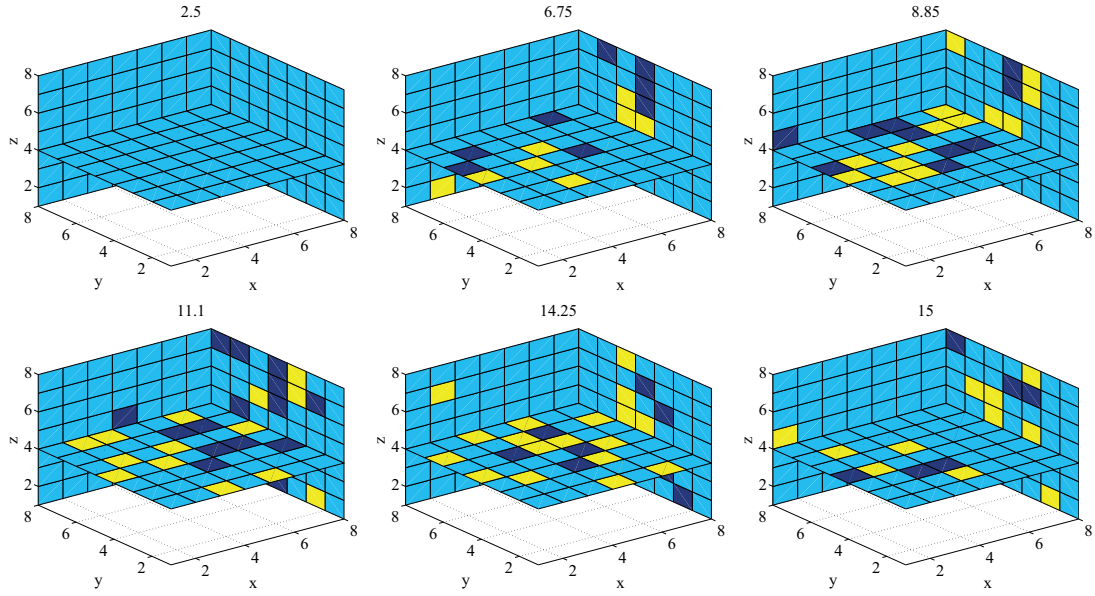

Figure 22: Taylor-Green vortex data: Cluster affiliation of analysis cells for different times $t \in \{2.5, 6.75, 8.85, 11.1, 14.25, 15\}$. Results for the optimal ($\mathbf{K}^* = 3, \mathbf{C}^* = 9$)-VX-solution of sub-sampling length $L = 1200$. The colours correspond to different clusters affiliations, yellow: γ_1, light blue: γ_2, dark blue: γ_3.

in the secondary components of the numerical flux correction terms, which are almost of no significance in the core model but have some influence in the wall model. These contributions are small compared to the dominating main components, but, apparently, meaningful in the sum.

5.2 Taylor-Green vortex flow

In Section 4.2, we have presented the results of the FEM-BV-VX framework applied to the Taylor-Green vortex flow of decaying turbulence. This flow is characterized by a temporal breakdown of anisotropic vortices, a development of turbulence and a final decay due to lack of mean shear. Our analysis approach was able to detect the structural changes in the flow patterns by adjusting the best-fit model in time and space. Fig. 22 gives an impression of the temporal evolution of the cluster association in the periodic box. It shows three normal slices through the $8\times8\times8$ cube of analysis cells, coloured by their cluster association. In the initial laminar phase, the model 2 is consistently active in all cells of the flow. It should be noted that during this time, the flux correction term is small, but not negligible, i.e. the active model is non-trivial. With the breakdown of the large vortices after around $t \approx 5$–6, models 1 and 3 are activated within the vortex, close to the core region. The outer region remains mostly at model 2, since the symmetry enforced by the periodic boundary conditions suppresses the development of isotropic small scale structures. After the transition to turbulence when a fully turbulent flow with inertial subrange according to Kolmogorov's $k^{-5/3}$ law has developed in the core region, the cluster association fluctuates in time, with mainly models 3 and 1 active. As the fluctuations subside with ongoing time, a reversion to the (laminar) model 2 is observed again.

A closer inspection of Fig. 22 and Figs. 18 and 19 raises two related issues that need to be investigated further. Firstly, while most of the cells close to the boundaries show little model dynamic, some (e.g. cell 69 in Fig. 18) show essentially the same behaviour as inner cells. Secondly, since the flow is governed by (anti-) symmetries about the centre and along planes aligned with the box axes, these symmetries should translate to the flux correction terms, the external factors and thus into the model dynamics. In Fig. 18, the cells $\{69, 77, 85, 93\}$ and $\{108, 116, 124\}$ as well as the x^+ and x^- columns show these symmetries. At a different $z = const.$ position (Fig. 19), no obvious symmetries in the model dynamics can be observed.

Fig. 23 shows the dependence of the fitted flux corrections on the length of the sampling vector L. It should be noted that while the fit indeed improves with a higher sampling rate, it does not capture the high frequency oscillations in the exact flux correction. As indicated in Table 3, the optimal model parameters depend strongly on L. In particular, with increasing sampling rate, the optimal number of model switches increases, and reaches the upper bound (imposed due to computational resources) of $C = 9$ for $L = 1200$. This fact might indicate that the global optimum in terms of L and C has not been found yet. An increase in both L and the upper bound on C is thus a possible candidate for a better model fit. Thus, the incomplete symmetry of the setup (cf. Section 3.2) and the differences in fitting quality between cells might explain the general loss in model symmetry and the behaviour in the boundary cells.

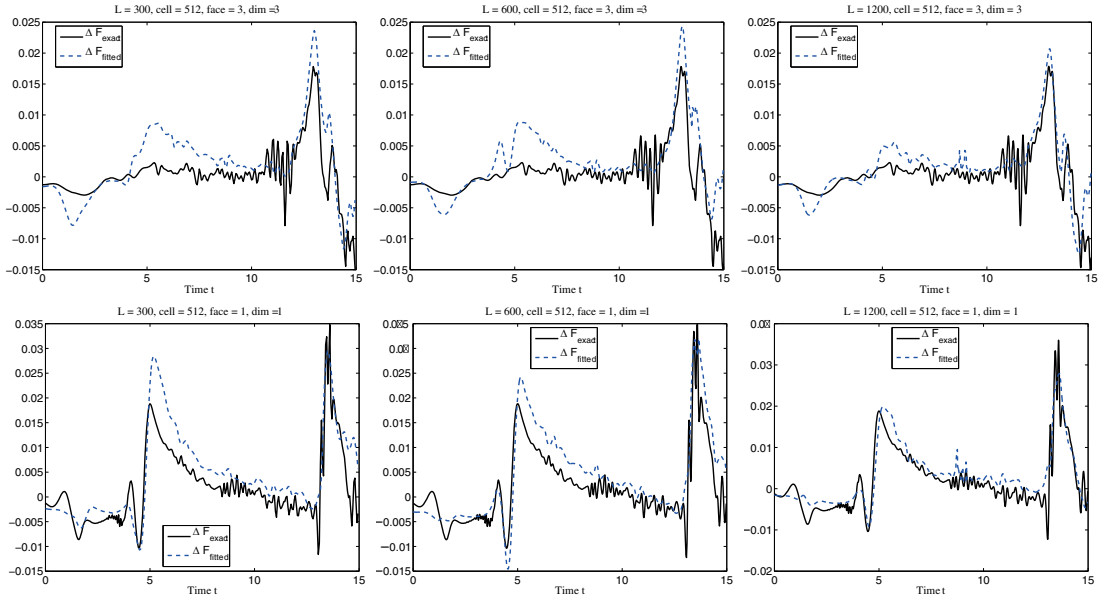

Figure 23: Taylor-Green vortex data: Exact corrections ΔF vs. fitted corrections. Results for the optimal parameters $\mathbf{K}^*$ and $\mathbf{C}^*$ as a function of the sub-samplings $L \in \{300, 600, 1200\}$ of the cell's time series. *top row:* z-momentum flux across z^+ face of cell 512, *bottom row:* x-momentum flux across x^+ face of cell 512.

Overall, our investigations have shown that our modelling approach through explicit dissipation terms can fit the exact flux corrections successfully. In addition, the analysis framework is capable of identifying changes in solution structure, and thus trigger model switches. This feature is of particular significance, as it allows the adaptation of the implicit or explicit modelling strategy based on the current solution.

6 Conclusion and outlook

In this paper, we have presented our work towards a stochastic LES closure approach. Our approach is based on advanced time series analysis techniques leading to a mixed deterministic-stochastic model formulation. The concept of the FEM-BV-VARX-formulation was used to reconstruct unresolved subgrid scale fluxes. This modelling approach was applied to two typical test cases of 3D DNS fluid flow data, i.e. the turbulent channel flow and the Taylor-Green vortex flow, to show its reconstruction capabilities. The turbulent channel flow data were computed by M. Uhlmann for an incompressible, isothermal fluid at Reynolds number $Re_\tau = 590$. For the analysis of the Taylor-Green vortex flow, a hybrid framework was created, that allows the simultaneous generation and comparison of DNS and LES data as model training parameters.

We mention here that our model approach must not be treated as an extended data analysis method only. In fact, we have presented a method for a data-based stochastic model-discrimination of implicit and explicit LES closures. The modified Akaike information criterion (mAIC), a further development of the AIC method by Horenko 2010b and Metzner et al. 2012 was used for identifying the best-fit stochastic subgrid scale model. To give the reader an estimate of this time-consuming procedure of model selection, 280,000 CPU-hours at a high performance computing cluster have been invested to identify the best model for the reconstruction of the subgrid scale fluxes from the high-dimensional data-sets of the turbulent channel flow test case. The features of the novel mAIC-metric particularly allow for a simultaneous data-based measure of quality and of complexity of the specific models without any a priori assumptions of the stochastic terms involved in. Furthermore, it allows us to identify details of the coarse grid modelling approach. In the Taylor-Green vortex flow test case, the Bayesian information criterion (BIC) has been used as information criteria.

For both test cases, we have identified the VX-model as the model of choice. This model does not consider auto-regressive terms. In the turbulent channel flow the model selection study resulted in a stationary, non-homogeneous model as the best-fit model. Thus, the channel flow data model deviates from standard models which are typically based on homogeneous statistical approaches only.

For the Taylor-Green vortex flow, a non-homogeneous, non-stationary VX-model has been identified as the best fit-model. It prescribes temporal changes of the cell-local models to account for developing physical structure of the underlying flow field. This feature highlights one of the strengths of our approach, in that a solution-adaptive model change can be detected to guarantee an optimal reconstruction. We found that the sampling frequency of the turbulent signal and the upper bound on the model persistence strongly influence the choice of optimal model. There are indications that due to the high temporal dynamics of this specific flow, an

increase in both the sampling frequency and the bound on model switches might lead to an even better fit.

Considering the mixed deterministic-stochastic model ansatz, it is called stochastic because the general model ansatz includes a stochastic noise term to model the statistics of the residuals left when only considering the determinstic part of the scheme. We, surprisingly, found that the deterministic part alone is good enough to fit the flux correction terms well and that the local stencil information may work well without added stochastic noise. The best-fit deterministic flux corrections agree very well despite the roughness of the coarse-grid data. This non-trivial result mentions also the role of deterministic LES closure approaches. Moreover, we found that the linear contribution to the closure incorporates a next-neighbour stencil on the coarse grid, and data of more distant cells are of no importance here.

As already stated above we here mention again that we are not primarily proposing two closure models. Rather, we are proposing a general approach to data-based determination of LES closures and validate this on two very different approaches related to standard LES and implicit LES. As discussed, we obtained interesting conclusions in both cases reflecting on both the flow physics and the modelling approaches. In addition to the above discussed topics, the outcome of our modelling approach sheds light on implicit LES models in the channel case, demonstrating that the generally successful and similar Adaptive Local Deconvolution Method (ALDM) approach may profit from explicit near-wall adjustment of the reconstruction weights. It, too, sheds light on classical LES closures in that we find reductions of model-to-DNS discrepancies in the Taylor-Green vortex flow case when time dependent regimes are explicitly accounted for.

The results which have been documented in this paper encourage us for the ambitious attempt at dynamic LES closure. As stated earlier, the paper describes several important results. We, however, see possible criticism as the optimization results are evaluated on a priori basis by visually comparing predicted fluxes with exact fluxes for selected cells and time steps. For the turbulent channel flow test case we analyzed the quantitative measure of the error norms. It is known that such results tell little about the nonlinear dynamic of a model in actual simulations. We, therefore, foresee the necessity of substantial further research into the construction of such closure. We will continue our strategy to reduce the classical closure problem to the faithful reconstruction of spatio-temporal fluctuations of the fluxes across grid cell interfaces. We, also, will make further use of the stochastic approach for the analysis of local flow features and will conduct a thorough comparison of the implicit-LES ansatz versus explicit-LES by coupling the stochastic based flux correction model to Finite Volume solvers.

In the future, we will continue our work on developing the closure strategy presented here for predictive modelling. Our route towards predictive modelling envisages a dynamic LES ansatz based on a multigrid closure approach similar to e.g., Germano et al. (1991) and Porté-Agel (2004). Here, a dynamic learning process would be able to autonomously select and operate model parameters for the construction of the subgrid scale surrogate closure models. The flux correction data would then be modelled using the most recent simulation data of the generated LES surrogate models instead of using DNS reference data. With that, the LES simulation itself would be the basis for determining the stochastic model parameters, and the model would then operate in a self-consistent way.

Acknowledgments

The study presented here summarizes the work performed by three workgroups in an interdisciplinary project funded by the German Research Foundation (DFG) within the priority program 1276 MetStroem (http://www.metstroem.de). Rupert Klein, Matthias Waidmann, and Thomas von Larcher at Freie Universität Berlin, Germany, DFG ref. no. KL 611/21, Illia Horenko and Philipp Metzner, Università della Svizzera Italiana, Switzerland, DFG ref. no. HO 4029/1, and Claus-Dieter Munz, Andrea Beck and Gregor Gassner at University of Stuttgart, Germany, DFG ref. no. MU 1319/14, gratefully acknowledge long-term support by DFG.

The turbulent channel flow data were generated in the early 2000s in an extended DNS study by Markus Uhlmann at the Potsdam-Institute for Climate Impact Research, Germany, within DFG-Project KL 611/10 using resources of the North-German Supercomputing Alliance (HLRN), Berlin, Germany. Markus Uhlmann is now Professor at the Institute for Hydromechanics, Karlsruhe Institute of Technology, Germany. The computer time consuming as well as storage consuming processing of the channel flow data has been performed at HLRN, too.

The Taylor-Green vortex computations were performed at the High Performance Computing Center (HLRS), Stuttgart, Germany.

The extensive best-model identification study based on the mAIC-metric was performed at the Swiss National Supercomputing Centre (CSCS) Switzerland.

Appendix

A Pre-Processing of the channel flow data

To determine the cell averages in the coarse Finite Volume grid cell centres, a fine Cartesian auxiliary grid, also with equidistant spacing in each spatial direction, is used, hereafter referred to as *fine grid*. The spatial resolution of this fine grid is similar to the resolution of the

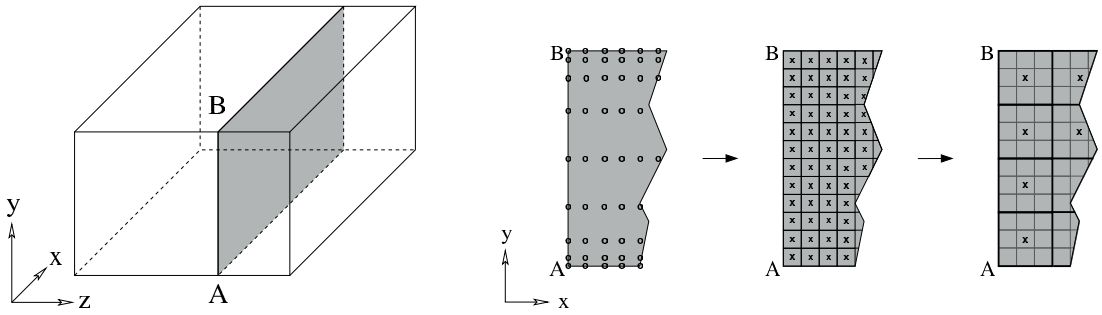

Figure 24: *Left*: sketch of a 2D (x, y)-slice. *Right*: transformation from the original grid with Chebyshev-distributed grid points in y-direction (left panel) to equidistant coarse grid cell average data (right panel) via fine grid cell average data (middle panel) with 3×3 fine grid cells within one coarse grid cell.

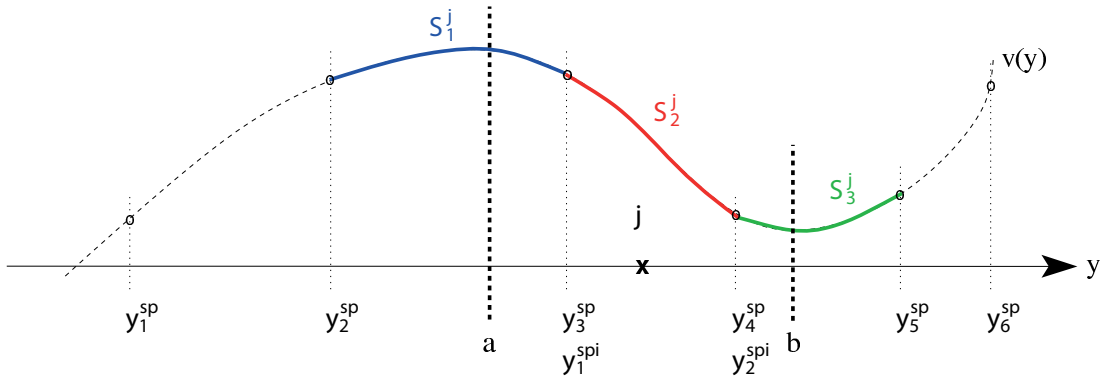

Figure 25: Re-sampling of fine grid cell average values of velocity data from non-equidistant grid points along the y-axis. Colours indicate the different S-terms given in (A.5).

grid of the previously restored non-equidistant velocity data and chosen such that an integer number of fine grid cells fit one coarse grid cell. Fig. 24 shows an example of the procedure for a 2D-sketch.

Finite Volume cell averages In the following we describe the re-sampling process of the velocity data which is used to determine the averaged velocity at the cell centres on both, the fine and the coarse Finite Volume grid, prior to the calculation of the particular fluxes.

Re-sampling: fine grid velocity data To obtain an equidistant distribution of the velocity data in wall-normal direction (along the y-axis) as well, a one dimensional 3-step operation, described in the following, is performed for each velocity component in each fine grid cell (e.g. cell j in Fig. 25). Due to the strong time consumption of this procedure, this process needs to be executed by use of parallel computations.

1. Spline Interpolation: the continuous solution is approximated via piecewise cubic spline interpolation (e.g., Munz and Westermann (2006)) of the Chebyshev-distributed velocity values in wall-normal direction. Due to this distribution of the velocity data many sample points are usually located within one fine grid cell close to the (solid) wall boundaries while it might happen that there is only one or even no sample point within a fine grid cell near the centre. In general, that, of course, depends strongly on the fine grid resolution.

   Let $n_{\mathrm{spi}}^{(j)}$ be the number of samples within a specific fine grid cell j and $n_{\mathrm{css}}^{(j)}$ the number of cubic spline segments used for approximation of the solution within cell j. Then at least one natural cubic spline segment is used to determine the integral average value of this fine grid cell in case no sample is located within the cell. Five samples and, thus, two cubic spline segments are used in case of $n_{\mathrm{spi}}^{(j)} = 1$, six samples (three cubic spline segments) in case of $n_{\mathrm{spi}}^{(j)} = 2$ (as illustrated in Fig. 25) and so on. Consequently, $n_{\mathrm{css}}^{(j)}$ depends on $n_{\mathrm{spi}}^{(j)}$ as well as on the number of additional samples $n_{\mathrm{spo}}^{(j)}$ outside of cell j yielding

$$n_{\mathrm{css}}^{(j)} = (n_{\mathrm{spi}}^{(j)} + n_{\mathrm{spo}}^{(j)}) - 3, \qquad \text{(A.1)}$$

   where $n_{sp}^{(j)} := (n_{\mathrm{spi}}^{(j)} + n_{\mathrm{spo}}^{(j)})$ is the total number of samples used for cell j. In general, four samples, two on each side of the fine grid cell, are used in the process, and thus $n_{\mathrm{spo}}^{(j)} = 4$ (cf. Fig. 25), and then $n_{\mathrm{css}}^{(j)} = n_{\mathrm{spi}}^{(j)} + 1$.

2. Integration: the integration of the i resulting cubic spline segments

$$s_i^{(j)}(y) = a_i^{(j)} y^3 + b_i^{(j)} y^2 + c_i^{(j)} y + d_i^{(j)} \qquad \text{(A.2)}$$

is performed analytically yielding the integral functions $S_i^{(j)}$ for the i spline segments of the current fine grid cell j

$$S_i^{(j)}(y) = \frac{a_i^{(j)}}{4} y^4 + \frac{b_i^{(j)}}{3} y^3 + \frac{c_i^{(j)}}{2} y^2 + d_i^{(j)} y + e_i^{(j)} \qquad \text{(A.3)}$$

3. Integral Average Value: the integral average values of the velocity components in fine grid cell j are determined via evaluation of the integral functions $S_i^{(j)}$ obtained in the previous step in the corresponding intervals within the interval $[a, b]$ (see Fig. 25). With the notation (*) $[g(y)]_p^q = (g(q) - g(p))$ this yields

$$\bar{v}_{\text{fine}}^{(j)} = \frac{1}{(b-a)} \left(\left[S_{ni+1}^{(j)}(y) \right]_{y_{ni}^{spi}}^{b} + \left[S_{ni}^{(j)}(y) \right]_{y_{ni-1}^{spi}}^{y_{ni}^{spi}} + \ldots + \left[S_2^{(j)}(y) \right]_{y_1^{spi}}^{y_2^{spi}} + \left[S_1^{(j)}(y) \right]_{a}^{y_1^{spi}} \right) \qquad \text{(A.4)}$$

This is also illustrated in Fig. 25 where $n_{\text{spi}}^{(j)} = 2$ and the resulting average value is

$$\bar{v}_{\text{fine}}^{(j)} = \frac{1}{(b-a)} \left(\left[S_3^{(j)}(y) \right]_{y_2^{spi}}^{b} + \left[S_2^{(j)}(y) \right]_{y_1^{spi}}^{y_2^{spi}} + \left[S_1^{(j)}(y) \right]_{a}^{y_1^{spi}} \right). \qquad \text{(A.5)}$$

The undetermined constants $e_i^{(j)}$ in (A.3) cancel while the integral functions are evaluated according to (*).

Re-sampling: coarse grid velocity data Once the velocity data are re-sampled on the fine grid, the integral average values of the velocity components in the coarse grid cells are determined by averaging the values in those fine grid cells which are located within the specific coarse grid, cf. Fig. 24.

Coarse grid cell face fluxes on fine grid time levels The re-sampling process described above results in velocity data sets of Finite Volume cell averages on two specific grids, a fine and a coarse grid, and enables us to calculate fluxes and flux corrections. In this paragraph, we describe the particular fluxes briefly, with F representing numerical fluxes (F_1, F_2, F_3) or flux averages (F_{ref}, F_{ex}) and $f(u)$ indicating an evaluation of the physical flux function based on state u. Note, that the numerical fluxes are all computed by using the same numerical flux function proposed in Hickel et al. (2006), and only the construction of the boundary traces changes with $F_{1,2,3}$.

1. Exact Flux (F_{ex}): to determine the exact flux F_{ex} across coarse grid cell faces

   (a) the equidistant fine grid velocity data are interpolated to obtain velocity values u^* at the coarse grid cell faces,

   (b) the non-linear part of the convective flux function is evaluated on the fine grid at coarse grid cell faces based on u^*, and

   (c) the fluxes at the coarse grid cell faces are determined via averaging over the K fine grid fluxes belonging to each corresponding coarse grid cell face

$$F_{\text{ex}} = \frac{1}{K} \sum_{k=1}^{K} f(u_k^*). \qquad \text{(A.6)}$$

This calculation is illustrated in Fig. 26 for a two dimensional grid with 3×3 fine grid cells per coarse grid cell.

2. Reference Flux (F_{ref}): for the reference flux over a cell face $j + \frac{1}{2}$ no state reconstruction or specific numerical flux function is used but the simple flux average

$$F_{\text{ref}} = \frac{1}{2} \left[f(u_j) + f(u_{j+1}) \right] \qquad \text{(A.7)}$$

is calculated.

3. 1st Order Flux (F_1): as in standard first order Finite Volume methods, here, the cell average state value is assumed to cover the whole grid cell and, thus, the values at the cell faces are assumed to be equal to the cell centre value. Consequently, no state reconstruction is needed. Note, that the flux is of 1st order in time but not in space as described below.

4. 2nd Order Flux (F_2): for obtaining the second order flux, F_2, piecewise linear state reconstruction at the cell faces is performed direction by direction based on the cell centre values as in standard second order Finite Volume methods, using a monotonized central limiter (van Leer, 1974) for slope limiting during the reconstruction.

5. 3rd Order Flux (F_3): for the third order flux F_3, state recovery at the cell faces is obtained via a third order WENO scheme by Shu (1997).

As already mentioned above, the numerical fluxes are then calculated by using always the same numerical flux function by Hickel et al.

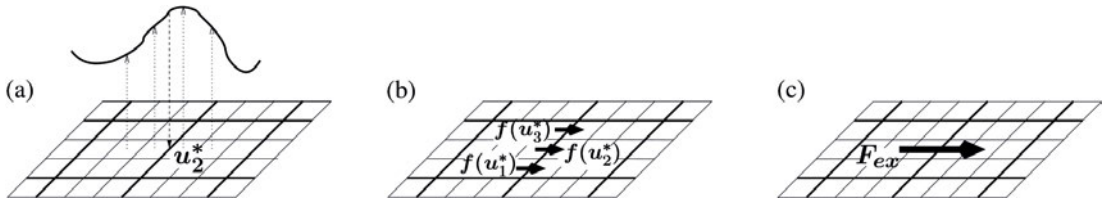

Figure 26: Example of exact flux (F_{ex}) computations: determination of state at coarse grid cell face via interpolation (a), evaluation of fine grid fluxes at coarse grid interface (b), and averaging to coarse grid cell face flux (c). Note, that in this example one coarse grid cell consists of 3×3 fine grid cells.

Time integration: coarse grid cell face fluxes on coarse grid time levels Although the different fluxes are determined at coarse grid cell faces there are now values for all these fluxes available at time levels corresponding to the original fine grid. Due to the well-known *CFL*-condition, cf. Courant et al. (1928), a single time step Δt for a numerical scheme can be larger on a coarser grid. To obtain fluxes over a time step corresponding to the coarse grid, integration is performed over the fluxes at fine grid time levels which are within the corresponding coarse grid time step. This is not necessary for the first and second order fluxes: in case of F_1 a constant flux over the whole coarse grid time step is assumed by simply taking the flux at the beginning of the time step as the average flux over the whole time step. For F_2, and also for F_{ref}, the averages of the fluxes at the beginning and at the end of the time step are calculated. However, for the higher order fluxes numerical integration needs to be performed: in case of F_3, first, a flux at intermediate time level $n + \frac{1}{2}$ is determined by third order Lagrange interpolation (cf. Munz and Westermann (2006)) to obtain a value at half time of time step $\Delta t = t^{n+1} - t^n$. Integration using the values at time levels n, $n + \frac{1}{2}$ and $n + 1$ is then done using Simpson's integration rule, c.f. Abramowitz and Stegun (1964). For the exact flux, F_{ex}, time integration is performed by a combination of Simpson's integration rule and Simpson's $3/8$ integration rule, Abramowitz and Stegun (1964), over the coarse grid time step using all the fluxes at all fine grid time levels available within the coarse grid time step (including start and end level of the time step).

B A Hybrid Discontinuous Galerkin-Finite Volume framework

For our modelling approach detailed in the Section 3.2 and described by (3.6) and (3.7), we need to determine a time series of flux corrections based on the exact fluxes and a number of quantities based on the grid resolved solution. For the channel flow we re-used existing DNS data, as described in Section 3.1. For the second test, we compute the DNS solution and the flux correction terms on the fly during the computation. This requires the creation of a suitable hybrid code framework, but allows a greater flexibility for the analysis of other flow scenarios at a later stage.

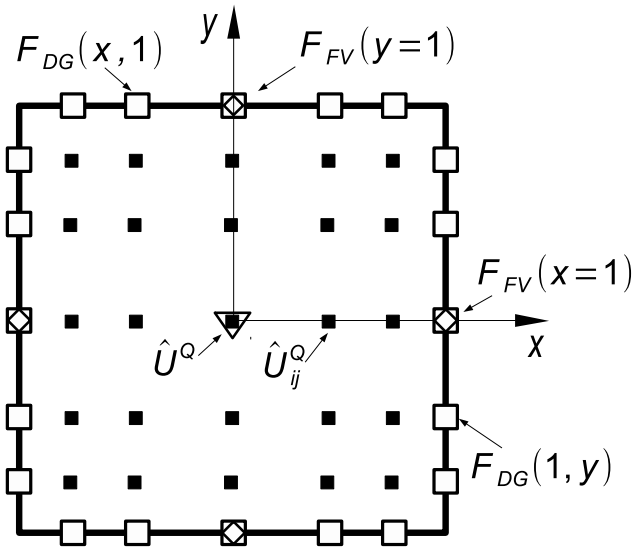

Figure 27: 2D solution and flux points of the combined DGSEM-FV framework for a reference cell: ■ DG Gauss points, □ DG boundary flux points, ▽ FV solution point, ⋄ FV flux points

Since DNS computations of turbulent flows require a highly efficient numerical and computational framework with low approximation errors, we choose a high order Discontinuous Galerkin Spectral Element method (DGSEM) as proposed e.g. by Kopriva (2009) as the base scheme for our DNS solver. In the method, the computational domain is divided into non-overlapping hexahedral elements. In each element, the solution vector $U(\vec{x}, t)$ containing the conserved variables is approximated by a polynomial tensor-product basis with degree N in each spatial direction

$$U(\vec{x},t) \approx U_h(\vec{x},t) = \sum_{i,j,k=0}^{N} \hat{U}_{\mathrm{ijk}}(t)\psi_{ijk}(\vec{x})$$
$$\psi_{ijk}(\vec{x}) = \ell_i(x)\ell_j(y)\ell_k(z)\,, \qquad \text{(B.1)}$$

with $\hat{U}_{ijk}(t)$ indicating the time-dependent nodal degrees of freedom, $\vec{x} = (x, y, z)^T$ and ℓ being the one-dimensional Lagrange interpolating polynomials of degree N. We choose Gauss integration points for the interpolation node set. Fig. 27 represents these points as filled squares. It should be noted that this approxima-

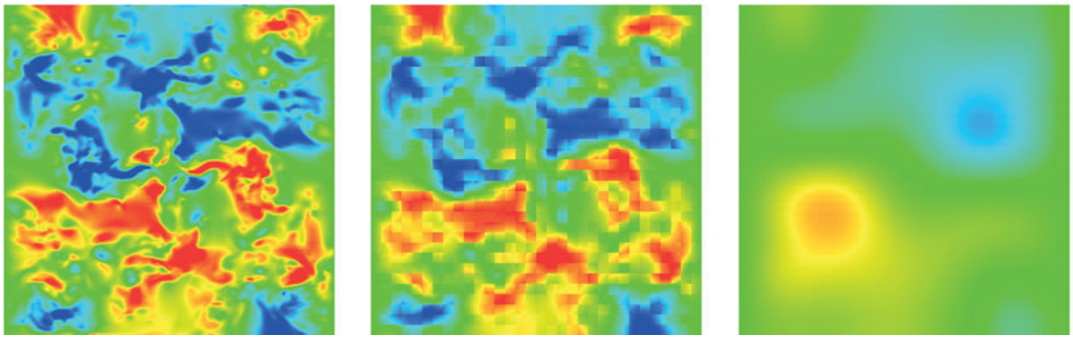

Figure 28: Contours of u-velocity on $z = const$ slice. *Left:* DNS solution, *middle:* FV $O(2)$ solution, reconstructed from DNS, *right:* FV $O(2)$ solution

tion is continuous within each element, but allowed to be discontinuous across element interfaces.

For a hyperbolic/parabolic evolution equation of the form

$$U_t + \nabla_x \cdot F(U, \nabla U) = \\ U_t + \nabla_x \cdot F^C(U) - \nabla_x \cdot F^V(U, \nabla U) = 0, \quad \text{(B.2)}$$

– for example the compressible Navier-Stokes equations with the solution vector U as the vector of the conserved variables $u = [\rho, \rho v_1, \rho v_2, \rho v_3, \rho e]$ as described above – the Discontinuous Galerkin formulation for the mixed first order system, written for one element Q and its surface ∂Q, reads

$$\int_Q (U_h)_t \, \varphi(\vec{x}) \, d\vec{x} = - \oint_{\partial Q} \left((\widehat{F^C \cdot n}) - (\widehat{F^V \cdot n}) \right) \varphi \, dS + \\ \int_Q F(U_h, W) \cdot \nabla_x \varphi(\vec{x}) \, d\vec{x},$$

$$\int_Q W \, \varphi(\vec{x}) \, d\vec{x} = \oint_{\partial Q} (\widehat{n * U_h}) \, \varphi \, dS - \int_Q U_h \, \nabla_x \varphi(\vec{x}) \, d\vec{x}, \quad \text{(B.3)}$$

where φ denotes the test function from the space of the basis functions, n denotes the outward pointing normal vector and $*$ the dyadic product. The terms F^C and F^V denote the Euler and viscous fluxes, respectively. The separation of the boundary contribution by partial integration allows us to introduce the numerical approximation of the flux traces $\widehat{(.)}$ at the grid cell interface. All flux traces have to be approximated by suitable flux functions for both the inviscid and viscous fluxes. Note that we have to prolongate the approximate solution from the interior Gauss points to integration points on cell surfaces to compute the trace integrals. These points are indicated by open squares in Fig. 27. Our code has been validated extensively and has been applied successfully for DNS and LES of turbulent flows. Extensive details about the method, its properties and our implementation can be found in Hindenlang et al. (2012); Gassner and Beck (2013); Gassner and Kopriva (2011).

Since we have thus established our code framework for computing the exact (DNS) fluxes $F_{\text{ex}}(u)$, we now need to evaluate the grid resolved quantities based on $\bar{u}$ for the model training described by (3.6). We have thus extended our code by including a second order Finite Volume formulation with linear cell-wise slope reconstruction. This Finite Volume formulation runs in parallel with the DGSEM formulation. Both discretizations share the same grid, i.e. each cell Q stores its associated DG solution and fluxes as well as their FV counterparts. Fig. 27 depicts this dualism of an exemplary cell. The plot has been reduced to a two dimensional case for a simpler visualization of the concept. The empty and filled squares denote the position of the DG points and the location of its boundary fluxes, while the triangle and open diamonds indicate the FV solution and the FV surface flux integration points. Thus, we realize the concept of a fine grid solution and a coarse grid approach not by using different meshes, but by changing the order of the approximation per cell and thus the associated degrees of freedom.

The general algorithm to compute the time series of the grid-dependent quantities in (3.6) is comprised of the following steps:

- For a given grid, the polynomial degree of the ansatz for the DG scheme is chosen sufficiently high to ensure a full resolution of the flow in a DNS sense.
- For each time step of the DG scheme Δt_{DG} which advances the DG solution $U_h^{DG}(t)$ to $U_h^{DG}(t + \Delta t)$, the exact fluxes $F_{\text{ex}}(u(t))_{ij}$ are computed on integration points (i, j) of the faces ∂Q_{face} (with $face = 1 \ldots 6$ for sides of a hexahedral elements) of an analysis cell Q. These exact fluxes are then integrated over their associated face ∂Q_{face} to give *one* flux vector $F_{\text{ex}}(u)$ per side.
- Parallel to this, the DG solution $U_h^{DG}(t)$ in each analysis cell and its neighbours is projected onto its mean value $U_h^{FV}(t)$ by

$$\int_Q U_h^{DG}(t) dQ = U_h^{FV}(t) \, |Q|, \quad \text{(B.4)}$$

where the quadrature of the DG polynomial is achieved by a sufficiently high order Gauss integra-

tion rule. Fig. 28 shows a DG solution and its FV projection in the left and middle plane at a given time t, while the right plot of Fig. 28 shows the FV $O(2)$ solution of an independent Finite Volume computation on the same grid at this time for reference.

- From these cell mean values $U_h^{FV}(t)$, a linear reconstruction operator computes $\bar{u}(t)$, which is then used to compute all the model input parameters in (3.6) and (3.7).
- In a final step, the flux correction is computed from $F_{\text{ex}}(u(t))$ and $F_{\text{central}}(\bar{u}(t))$ and stored together with the model input parameters in a file.
- The DG scheme then updates the DNS solution to $U_h^{DG}(t + \Delta t)$, and the cycle repeats.

References

Abramowitz, M., I. Stegun (Eds.), 1964: Handbook of Mathematical Functions with Formulas, Graphs, and Mathematical Tables. – NBS Applied Mathematics Series **55**, National Bureau of Standards, Washington, DC, USA.

Akaike, H., 1974: A new look at the statistical model identification. – IEEE Trans. Automatic Control **19**, 716–723.

Blume, C., K. Matthes, I. Horenko, 2012: Supervised learning approaches to classify stratospheric warming events. – J. Atmos. Sci. **69**, 1824–1840.

Brachet, M., 1991: Direct simulation of three-dimensional turbulence in the Taylor–Green vortex. – Fluid Dyn. Res. **8**, 1–8.

Brachet, M.E., D.I. Meiron, S.A. Orszag, B.G. Nickel, R.H. Morf, U. Frisch, 1983: Small-scale structure of the Taylor–Green vortex. – J. Fluid Mech. **130**, 411–452.

Brockwell, P., R. Davis, 2002: Introduction to Time Series and Forecasting. – Springer, Berlin.

Burnahm, K., D. Anderson, 2002: Model Selection and Multimodel Inference. – Springer, Berlin.

Courant, R., K. Friedrichs, H. Lewy, 1928: Über die partiellen Differenzengleichungen der mathematischen Physik. Math. Ann., **100**, 32–74 (in German).

Denaro, F., G. De Stefano, 2011: A new development of the dynamic procedure in large-eddy simulation based on a Finite Volume integral approach. Application to stratified turbulence. – Theor. Comput. Fluid Dyn. **25**, 315–355.

Domaradzki, J., E. Saiki, 1997: A subgrid-scale model based on the estimation of unresolved scales of turbulence. – Phys. Fluids **9**, 1–17.

Drikakis, D., C. Fureby, F.F. Grinstein, D. Youngs, 2007: Simulation of transition and turbulence decay in the Taylor–Green vortex. – J. Turb. **8**, 1–12.

Franzke, C., D. Crommelin, A. Fischer, A. Majda, 2007: A hidden markov model perspective on regimes and metastability in atmospheric flows. – J. Climate **21**, 1740–1757.

Franzke, C., I. Horenko, A. Majda, R. Klein, 2009: Systematic metastable atmospheric regime identification in an AGCM. – J. Atmos. Sci **66**, 1997–2012.

Gassner, G., A.D. Beck, 2013: On the accuracy of high-order discretizations for underresolved turbulence simulations. – Theor. Comput. Fluid Dyn. **27**, 221–237.

Gassner, G., D. Kopriva, 2011: Comparison of the Gauss and Gauss-Lobatto discontinuous Galerkin Spectral Element Method for wave propagation problems. – SIAM J. Scientific Computing **33**, 2560–2579.

Germano, M., P. Piomelli, P. Moin, W. Cabot, 1991: A dynamic subgrid-scale eddy viscosity model. – Phys. Fluids A **3**, 1760–1766.

Hickel, S., N. Adams, J. Domaradzki, 2006: An adaptive local deconvolution method for implicit LES. – J. Comput. Phys. **213**, 413–436.

Hindenlang, F., G. Gassner, C. Altmann, A. Beck, M. Staudenmaier, C.-D. Munz, 2012: Explicit discontinuous Galerkin methods for unsteady problems. – Comp. Fluids **61**, 86–93.

Horenko, I., 2010a: On clustering of non-stationary meteorological time series. – Dyn. Atmos. Ocean **49**, 164–187.

Horenko, I., 2010b: On identification of nonstationary factor models and its application to atmospherical data analysis. – J. Atmos. Sci. **67**, 1559–1574.

Jimenez, J., P. Moin, 1991: The minimal flow unit in near-wall turbulence. – J. Fluid Mech. **225**, 213–240.

Kim, J., P. Moin, R. Moser, 1987: Turbulence statistics in fully developed channel flow at low Reynolds number. – J. Fluid Mech. **177**, 133–166.

Klein, R., M. Uhlmann, 2000: Projektbeschreibung zum Großprojektantrag für den Parallelrechner T3E des ZIB (in German). – http://www-turbul.ifh.uni-karlsruhe.de/uhlmann/reports/trans2.pdf.

Kolmogorov, A., 1941: The local structure of turbulence in incompressible viscous fluid for very large Reynolds number. – C.R. Acad. Sci. U.S.S.R. **30**, 301.

Kolmogorov, A., 1962: A refinement of previous hypothesis concerning the local structure of turbulence in a viscous incompressible fluid at high Reynolds number. – J. Fluid Mech. **13**, 82–85.

Kopriva, D.A., 2009: Implementing Spectral Methods for Partial Differential Equations. – Springer.

Krolzig, H.-M., 2000: Predicting Markov-Switching Vector Autoregressive Processes. Economics Series Working Papers 2000-W31, University of Oxford, Department of Economics.

Leith, C., 1990: Stochastic backscatter is a subgrid-scale model: plane shear mixing layer. – Phys. Fluids A **2**, 297–299.

Lesieur, M., 1987: Turbulence in Fluids: Stochastic and Numerical Modelling – Martinus Nijhoff, Dordrecht, The Netherlands.

Liu, S., C. Meneveau, J. Katz, 1994: On the properties of similarity subgrid-scale models as deduced from measurements in a turbulent jet. – J. Fluid Mech. **275**, 83–91.

Majda, A., C. Franzke, A. Fischer, D. Crommelin, 2006: Distinct metastable atmospheric regimes despite nearly gaussian statistics: A paradigm model. – PNAS **103**, 8309–8314.

McQuarrie, A., C.-L. Tsai, 1998: Regression and Time Series Model Selection – World Scientific, New Jersey.

Metzner, P., L. Putzig, I. Horenko, 2012: Analysis of persistent non-stationary time series and applications. – CAMCoS **7**, 175–229.

Misra, A., D. Pullin, 1997: A vortex-based subgrid stress model for large-eddy simulation. – Phys. Fluids **8**, 2443–2454.

Moser, R., J. Kim, N. Mansour, 1999: Direct numerical simulation of turbulent channel flow up to $\text{Re}_\tau = 590$. – Phys. Fluids **11**, 943–945.

Munz, C.-D., T. Westermann, 2006: Numerische Behandlung gewöhnlicher und partieller Differenzialgleichungen. – Springer, Berlin.

Oboukhov, A., 1962: Some specific features of atmospheric turbulence. – J. Fluid Mech. **13**, 77–81.

O'Kane, T., R. Matear, M. Chamberlain, J. Risbey, I. Horenko, B. Sloyan, 2012: Low frequency variability in an couped ocean-sea ice general circulation model of the southern ocean. – ANZIAM J. **54**, C200–C216.

O'Kane, T., J. Risbey, C. Franke, I. Horenko, D. Monselesan, 2013a: Changes in the metastability of the midlatitude southern hemisphere circulation and the utility of nonstationary cluster analysis and split-flow blocking indices as diagnostic tools. – J. Atmos. Sci. **70**, 824–842.

O'Kane, T., R. Matear, M. Chamberlain, J. Risbey, B. Sloyan, I. Horenko, 2013b: Decadal variability in an OGCM southern ocean: Intrinsic modes, forced modes and metastable states. – Ocean Modelling **69**, 1–21.

Pope, S.B., 2000: Turbulent Flows. – Cambridge University Press, Cambridge, UK.

Porté-Agel, F., 2004: A scale-dependent dynamic model for scalar transport in large-eddy simulations of the atmospheric boundary layer. – Bound.-Layer Meteor. **112**, 81–105.

Roe, P., 1981: Approximate riemann solvers, parameter vectors, and difference schemes. – J. Comput. Phys. **43**, 357–372.

Rogallo, R., P. Moin, 1984: Numerical simulation of turbulent flows. – Ann. Rev. Fluid. Mech **16**, 99–137.

Sabel'nikov, V., A. Chtab-Desportes, M. Gorokhovski, 2011: New sub-grid stochastic acceleration model in LES of high-Reynolds-number flows. – Euro. Phys. J.B. **80**, 177–187.

Sagaut, P., 2006: Large Eddy Simulation for Incompressible Flows. – Springer, Berlin.

Schumann, U., 1995: Stochastic backscatter of turbulence energy and scalar variance by random subgrid-scale fluxes. – Proc. R. Soc. Lond. Ser. A **451**, 293–318.

Scotti, A., C. Meneveau, 1999: A fractal model for Large Eddy Simulation of turbulent flows. – Physica D **127**, 198–232.

Shu, C.-W., 1997: Essentially non-oscillatory and weighted essentially non-oscillatory schemes for hyperbolic conservation laws. – Tech. Rep. 97–65, ICASE, NASA Langley Research Center, Hampton, VA.

Smagorinsky, J., 1963: General circulation experiments with the primitive equations. i. the basic experiment. – Mon. Wea. Rev. **91**, 99.

Taylor, G.I., A.E. Green, 1937: Mechanism of the Production of Small Eddies from Large Ones. – Proc. R. Soc. Lond. A, Mathematical and Physical Sciences **158**, 499–521.

Toro, E., 1999: Riemann Solvers and Numerical Methods for Fluid Dynamics – Springer, Dordrecht.

Uhlmann, M., 2000a: Generation of a temporally well-resolved sequence of snapshots of the flow-field in turbulent plane channel flow. – Published online, http://www-turbul.ifh.uni-karlsruhe.de/uhlmann/reports/produce.pdf (accessed at 11.12.2014).

Uhlmann, M., 2000b: Generation of initial fields for channel flow investigation. Intermediate Report. – Published online, http://www-turbul.ifh.uni-karlsruhe.de/uhlmann/home/report.html (accessed at 11.12.2014).

Uhlmann, M., 2000c: The need for de-aliasing in a Chebyshev pseudo-spectral method. Technical Note No. 60. – Published online, http://www-turbul.ifh.uni-karlsruhe.de/uhlmann/reports/dealias.pdf (accessed at 11.12.2014).

van Leer, B., 1974: Towards the ultimate conservative difference scheme. ii. monotonicity and conservation combined in a second-order scheme. – J. Comput. Phys. **14**, 361–370.

Zamansky, R., I. Vinkovic, M. Gorokhovski, 2013: Acceleration in turbulent channel flow: universalities in statistics, subgrid stochastic models and an application. – J. Fluid Mech. **721**, 627–668.